Fast Multiscale Neighbor Embedding

Cyril de Bodt, Dounia Mulders, Michel Verleysen, *Fellow, IEEE*, and John Aldo Lee

***Abstract*— Dimension reduction (DR) computes faithful low-dimensional (LD) representations of high-dimensional (HD) data. Outstanding performances are achieved by recent neighbor embedding (NE) algorithms such as t-SNE, which mitigate the curse of dimensionality. The single-scale or multiscale nature of NE schemes drives the HD neighborhood preservation in the LD space (LDS). While single-scale methods focus on single-sized neighborhoods through the concept of perplexity, multiscale ones preserve neighborhoods in a broader range of sizes and account for the global HD organization to define the LDS. For both single-scale and multiscale methods, however, their time complexity in the number of samples is unaffordable for big data sets. Single-scale methods can be accelerated by relying on the inherent sparsity of the HD similarities they involve. On the other hand, the dense structure of the multiscale HD similarities prevents developing fast multiscale schemes in a similar way. This article addresses this difficulty by designing randomized accelerations of the multiscale methods. To account for all levels of interactions, the HD data are first subsampled at different scales, enabling to identify small and relevant neighbor sets for each data point thanks to vantage-point trees. Afterward, these sets are employed with a Barnes–Hut algorithm to cheaply evaluate the considered cost function and its gradient, enabling large-scale use of multiscale NE schemes. Extensive experiments demonstrate that the proposed accelerations are, statistically significantly, both faster than the original multiscale methods by orders of magnitude, and better preserving the HD neighborhoods than state-of-the-art single-scale schemes, leading to high-quality LD embeddings. Public codes are freely available at https://github.com/cdebodt.**

***Index Terms*— Barnes–Hut (BH), dimensionality reduction, multiscale methods, neighbor embedding (NE), t-SNE, vantage-point trees.**

Manuscript received April 17, 2019; revised December 8, 2019, May 31, 2020, and October 21, 2020; accepted November 25, 2020. Date of publication December 25, 2020; date of current version April 5, 2022. The work of Cyril de Bodt, Dounia Mulders, and John Aldo Lee was supported by the Fonds de la Recherche Scientifique-FNRS. Cyril de Bodt and Dounia Mulders are Research Fellows of the Fonds de la Recherche Scientifique-FNRS. John Aldo Lee is a Senior Research Associate with the FNRS. *(Corresponding author: Cyril de Bodt.)*

Cyril de Bodt is with the Human Dynamics Group, Massachusetts Institute of Technology (MIT) Media Lab, Cambridge, MA 02139 USA, and also with the Institute for Information and Communication Technologies, Electronics and Applied Mathematics (ICTEAM), Electrical Engineering Department (ELEN), Université catholique de Louvain (UCLouvain), 1348 Louvain-la-Neuve, Belgium (e-mail: cdebodt@mit.edu, cyril.debodt@uclouvain.be).

Dounia Mulders is with Fiete Lab, Department of Brain and Cognitive Sciences, Massachusetts Institute of Technology (MIT), Cambridge, MA 02139 USA, and also with the Institute for Information and Communication Technologies, Electronics and Applied Mathematics (ICTEAM), Electrical Engineering Department (ELEN), Université catholique de Louvain (UCLouvain), 1348 Louvain-la-Neuve, Belgium (e-mail: dmulders@mit.edu, dounia.mulders@uclouvain.be)

Michel Verleysen and John Aldo Lee are with the Institute for Information and Communication Technologies, Electronics and Applied Mathematics (ICTEAM), Electrical Engineering Department (ELEN), Université catholique de Louvain (UCLouvain), 1348 Louvain-la-Neuve, Belgium (e-mail: michel.verleysen@uclouvain.be; john.lee@uclouvain.be).

Color versions of one or more figures in this article are available at https://doi.org/10.1109/TNNLS.2020.3042807.

Digital Object Identifier 10.1109/TNNLS.2020.3042807

I. Introduction

DIMENSIONALITY reduction (DR) represents high-dimensional (HD) data sets into low-dimensional (LD) spaces, mostly for exploratory visualization or to dismiss the curse of dimensionality [1]. This curse encompasses the inherent difficulties to cope with HD data and motivated the development of adequate approaches to extract meaningful LD features [2], [3]. In visualization context, the relevance of a LD embedding is typically related to the HD neighborhood preservation. Mappings from HD to LD coordinates [1] formalize this neighborhood preservation principle in the context of paradigms, such as the reproduction of distances [4] or neighborhoods [5], [6]. Linear projections of the HD vectors include early principal component analysis (PCA) [7] and classical metric multidimensional scaling (MDS) [4], driven by the variance or dot product preservation. Nonlinear metric MDS extensions [8] define (weighted) distance preservation schemes relying on either Euclidean or approximated geodesic measures [9]. Affinity matrices may also be computed to guide the LD embedding tuning [10], [11]. However, these approaches are hardly superior to the older methods in visualization tasks [1], [12], [13], potentially because they can be expressed as classical MDS applied in an unknown feature space [14]. Distance-preserving schemes are particularly affected by the norm concentration phenomenon [15], which leads pairwise distances to become more and more similar as the dimension increases [16]. Meanwhile, neighbor embedding (NE) techniques as stochastic neighbor embedding (SNE) [6] and variants [13], [17] alleviate this phenomenon by matching neighbor probability distributions defined in both spaces to compute the LD points [16]. The resulting outstanding performances motivated developing alternative SNE-based models, with heavy-tailed distributions as in t-SNE [13], [18], [19], divergence mixtures as cost functions [17], [20], [21], missing data management [22], enhanced optimization [23]–[26], and so on.

Originally, NE methods required the user to specify some perplexity for the neighborhood probability distributions, resulting in preservation oriented toward neighborhoods of the corresponding size. These methods may hence be viewed as single scale, with fixed resolution. More recently, multiscale NE approaches were introduced by combining neighborhood probabilities tuned at various data scales [27], [28], leading to meta-parameter-free techniques. Compared with their single-scale counterparts, the multiscale schemes substantially better preserve neighborhoods of all sizes due to their ability to consider both local and global structures while computing the LD embedding. This enables, for instance, to reproduce small neighborhoods as well as or better than t-SNE while considerably improving the preservation of larger ones [27].

Despite their impressive results, single-scale and multiscale NE methods, respectively, have $\mathcal{O}(N^2)$ and $\mathcal{O}(N^2 \log N)$ time

complexity when employed with N data samples. Although the logarithmic factor further induced by the multiscale behavior has a minor impact, the quadratic dependence is not suited to big data sets and confines the use of NE methods to a few thousands of data points. An obvious workaround is to employ an NE method solely on a small random subset of the database, enabling its visualization for exploratory analysis. However, analyzing a reduced part of a data set often only reveals a limited fraction of the HD data relationships [29]. Another option is to use the HD and LD positions of the selected data samples to project the remaining data points after learning a parametric function between the HD space and LD space (LDS) [30], [31]. Nevertheless, learning such mappings is typically difficult since the NE method only processes a small part of the database [32], hence ignoring the information carried by most of the data points on the underlying HD structures [13]. Some studies experimentally show that applying NE methods on a subset of a database poorly generalizes as it largely neglects the HD data interactions [33], affecting the projection quality of the remaining samples and altering the structure of the data. Considering big data sets is further demonstrated to always be advantageous to tune visualizations, regardless of whether the whole database or only a portion needs to be analyzed [33]. Therefore, some works attempt to incorporate information from the entire data structure when visualizing a part of the samples, such as landmark t-SNE [13]. However, while preventing to observe the whole database, this approach entails considerable running times and memory requirements [33].

For these reasons, lower complexity approximations were introduced for single-scale methods, either relying on tree-based computations [32], [33], fast multipole methods (FMMs) [34], negative sampling techniques (NSTs) [35], or Gaussian mixture modeling approximations [29]. Although they effectively reduce computation times by reaching near-linear time complexity with respect to the number of data samples, Gaussian mixtures are typically difficult to tune in (very) HD spaces [36] and require to determine their number of components. A poor tuning or an inadequate number of mixture components deteriorates the quality of the HD modeling and, hence, the LD embedding. On the other hand, tree-based schemes, FMMs and NSTs, achieve impressive performances in terms of both quality and speedup, ensuing in methods with $\mathcal{O}(N \log N)$ and $\mathcal{O}(N)$ time complexity, provided that the HD neighbor probabilities can be sparsely encoded. The tree-based algorithms and FMMs poorly scale with the LD dimension, but the latter is typically as small as 2 or 3 for visualization purposes. However, the sparsity of the HD neighbor probability distributions is a key ingredient of tree-based methods, FMMs and NSTs. This fits the single-scale framework well, in which the neighbor probability distributions remain local around the data points, but not the multiscale one. Indeed, multiscale neighbor probability distributions span much larger levels of data organization to account for both local and global neighboring structures when tuning the LD embedding. This defines dense neighbor probability distributions, preventing to accelerate multiscale NE methods as the single-scale ones.

This article develops fast multiscale NE schemes with $\mathcal{O}\big(N \log^2 N\big)$ time complexity instead of $\mathcal{O}\big(N^2 \log N\big)$, able to manage large-scale databases with hundreds of thousands of data points for visualization. Appropriate neighbor sets are first computed for all samples using vantage-point trees defined on random subsamplings of the data set at all scales. This enables preserving the multiscale behavior of the methods by accounting for global data structures in the obtained neighbor sets. The cost function of the considered multiscale scheme is then minimized using these sets with a Barnes–Hut (BH) algorithm to efficiently approximate the LD data interactions and avoid LD crushing phenomena, i.e., overlapping LD points. Simulations on numerous data sets evidence that the proposed fast multiscale methods outperform state-of-the-art single-scale approaches such as t-SNE in terms of LD embedding quality quantified using neighborhood preservation criteria while at the same time being considerably faster than nonaccelerated NE algorithms. These results are statistically significant with respect to the random subsamplings of the data. Free codes are publicly available online (https://github.com/cdebodt), enabling to easily employ the presented algorithms.

This article is organized as follows. Section II reviews NE methods in both single-scale (see Section II-A) and multiscale (see Section II-B) settings. Section III first describes lower complexity approximations for fast single-scale schemes (see Section III-A) and then introduces the proposed randomized multiscale accelerations (see Section III-B). Section IV details the experimental results comparing the performances of (single-scale) t-SNE, multiscale SNE, and multiscale t-SNE with their respective fast versions on several data sets, in terms of both computation time and DR quality, for varying values of the BH algorithm meta-parameter. The accelerated methods are also validated on large databases on which it is unaffordable to employ the original, nonfast NE algorithms. Section V draws final conclusions.

II. Neighbor Embedding

DR aims to map HD data sets in LDSs by best preserving their structure. The data points HD neighborhoods should hence be well reflected by the LD ones. In this view, rigid distance preservation methods are outperformed by the successful NE approaches [1]. They are based on the concept of neighbor probabilities, first introduced by SNE [6] and refined in more recent multiscale techniques, yielding impressive performances [27]. SNE and its t-SNE variant are first reviewed in Section II-A. Their multiscale extensions are then presented in Section II-B.

A. Single-Scale Methods

Given a set $\boldsymbol{\Xi} = \{\boldsymbol{\xi}_i\}_{i=1}^N$ of N points lying in an M-dimensional space (HDS), let $\mathbf{X} = \{\mathbf{x}_i\}_{i=1}^N$ refer to its representation in a P-dimensional space, termed the LDS, with $P \leq M$. The distances between the ith and jth points are denoted by δ_{ij} and d_{ij} in the HDS and LDS respectively. Single-scale pairwise HD and LD similarities are defined by SNE for each $i \in \mathcal{I} := \{1, \ldots, N\}$ and $j \in \mathcal{I}\backslash\{i\}$

$$\sigma_{ij\star} = \frac{\exp(-\pi_{i\star}\delta_{ij}^2/2)}{\sum_{k\in\mathcal{I}\backslash\{i\}} \exp(-\pi_{i\star}\delta_{ik}^2/2)}, \quad \sigma_{ii\star} = 0 \tag{1}$$

$$s_{ij\star} = \frac{\exp(-p_{i\star}d_{ij}^2/2)}{\sum_{k\in\mathcal{I}\backslash\{i\}} \exp(-p_{i\star}d_{ik}^2/2)}, \quad s_{ii\star} = 0. \tag{2}$$

A binary search sets the precision $\pi_{i\star}$ to obtain a user-provided perplexity $K_\star$ for the distribution $\boldsymbol{\sigma}_{i\star} = \{\sigma_{ij\star}, j \in \mathcal{I}\backslash\{i\}\}$

$$\pi_{i\star} \text{ s.t. } \log K_\star = -\sum_{j\in\mathcal{I}\backslash\{i\}} \sigma_{ij\star} \log \sigma_{ij\star}. \tag{3}$$

In practice, only a finite maximum number of iterations is tolerated during the binary search, to avoid infinite loops when it is impossible to tune $\pi_{i\star}$ in order to obtain a perplexity $K_\star$, for instance when the HD distances in $\{\delta_{ij}, j \in \mathcal{I}\backslash\{i\}\}$ are all equal. The LD precisions $p_{i\star}$ are fixed to 1. The soft Gaussian neighborhood size is quantified by the perplexity, meaning that (1) and (2) can be interpreted as probabilities for j of being a neighbor of i in the HDS and LDS. The star index in $K_\star$ is for consistency with Section II-B. To compute $\mathbf{X}$, the sum over $i \in \mathcal{I}$ of the Kullback–Leibler (KL) divergences between the distributions $\boldsymbol{\sigma}_{i\star}$ and $\boldsymbol{s}_{i\star} = \{s_{ij\star}, j \in \mathcal{I}\backslash\{i\}\}$

$$C_\star = \sum_{i\in\mathcal{I}, j\in\mathcal{I}\backslash\{i\}} \sigma_{ij\star} \log(\sigma_{ij\star}/s_{ij\star}) \tag{4}$$

is minimized by SNE through gradient-based optimization [6].

Besides symmetrizing the similarities, t-SNE uses a Student t-distribution with one degree of freedom in the LDS, circumventing the crowding problem [13], which refers to the difficulty to reproduce data similarities from large HD volumes to exponentially smaller LD ones: for $i \in \mathcal{I},\ j \in \mathcal{I}\backslash\{i\}$

$$\tau_{ij\star} = (\sigma_{ij\star} + \sigma_{ji\star})/(2N), \quad \tau_{ii\star} = 0 \tag{5}$$

$$t_{ij} = \frac{(1 + d_{ij}^2)^{-1}}{\sum_{k\in\mathcal{I}, l\in\mathcal{I}\backslash\{k\}} (1 + d_{kl}^2)^{-1}}, \quad t_{ii} = 0. \tag{6}$$

The t-SNE cost function remains as in SNE

$$C_{t\star} = \sum_{i\in\mathcal{I}, j\in\mathcal{I}\backslash\{i\}} \tau_{ij\star} \log(\tau_{ij\star}/t_{ij}). \tag{7}$$

Other variants of SNE were defined by modifying its cost function using mixtures of divergences [20], such as the neighborhood retrieval visualizer (NeRV) [17] and Jensen–Shannon embedding (JSE) [21]. For all these SNE-based methods, evaluating the cost function or its gradient scales in $\mathcal{O}(N^2)$ since it requires computing all similarities.

B. Multiscale Methods

Small and arbitrary perplexities $K_\star$ are typically used in SNE, inducing local HD distance focus in (1), mainly preserving small neighborhoods. Indeed, most HD similarities are infinitesimal, hiding the associated LD similarities to the SNE cost function. Such local distance transformations, hence, neglect the mid- and large-scale interactions when designing the embedding global structure. The long-range neighborhood preservation is therefore considerably affected. On the other hand, nearly uniform HD similarities result from too large perplexities, harming the small neighborhood preservation.

However, the multiscale SNE method [27] combines various SNE similarities relying on increasing perplexities, to model both local and global trends and to retrieve several data scales simultaneously. Single-scale similarities are now indexed using a scale counter h, for $i \in \mathcal{I}$ and $j \in \mathcal{I}\backslash\{i\}$, as

$$\sigma_{ijh} = \frac{\exp\left(-\pi_{ih}\delta_{ij}^2/2\right)}{\sum_{k\in\mathcal{I}\backslash\{i\}} \exp\left(-\pi_{ih}\delta_{ik}^2/2\right)}, \quad \sigma_{iih} = 0 \tag{8}$$

$$s_{ijh} = \frac{\exp\left(-p_{ih}d_{ij}^2/2\right)}{\sum_{k\in\mathcal{I}\backslash\{i\}} \exp\left(-p_{ih}d_{ik}^2/2\right)}, \quad s_{iih} = 0. \tag{9}$$

Multiscale similarities average the single-scale ones as

$$\sigma_{ij} = H^{-1}\sum_{h=1}^{H} \sigma_{ijh}, \quad s_{ij} = H^{-1}\sum_{h=1}^{H} s_{ijh} \tag{10}$$

where the number of scales is denoted by H. One can set precisions π_{ih} as in SNE using perplexities summarizing the whole data range, selected in a data-driven way without any user intervention. Indexed perplexities are introduced as $K_h = 2^{h-1}K_1$ [27], with a small base perplexity such as $K_1 = 2$ and $1 \le h \le H = \lfloor \log_2(N/K_1) \rceil$, where $\lfloor\cdot\rceil$ represents rounding. The entropy of the HD similarity distributions hence linearly increases across scales. The LD precisions $p_{ih} = p_h = {K_h}^{-2U/P}$ follow the exponential growth of the perplexities, with U fixed from the HD precisions as in [27].

Multiscale SNE keeps the SNE cost function, developing as

$$C = -\sum_{i\in\mathcal{I}, j\in\mathcal{I}\backslash\{i\}} \sigma_{ij} \log s_{ij} \tag{11}$$

since the entropy of the HD similarities does not depend on $\mathbf{X}$. On the other hand, multiscale t-SNE [28] minimizes

$$C_t = \sum_{i\in\mathcal{I}, j\in\mathcal{I}\backslash\{i\}} \tau_{ij} \log \frac{1}{t_{ij}}, \text{ with } \tau_{ij} = \frac{\sigma_{ij} + \sigma_{ji}}{2N}. \tag{12}$$

Multiscale NeRV and JSE can also be defined [27], by replacing their single-scale similarities with multiscale ones.

The optimization of SNE-like methods turns out to be tough [6], [17], [23], [26], in particular when small perplexities are considered since they induce high-frequency oscillations in the cost functions [27]. Heuristics to attempt avoiding shallow local minima are usually helpful and include early exaggeration [13] and multiscale optimization [27], which starts the minimization with the largest scale and then progressively introduces the smaller ones.

The $\mathcal{O}(\log N)$ scales entail a $\mathcal{O}(N^2 \log N)$ time complexity for the multiscale NE schemes. While single-scale algorithms best reproduce neighborhood sizes close to or smaller than $K_\star$ but poorly preserve larger ones, broader ranges of neighborhoods are retrieved by the multiscale methods. This enables retaining both local and global data structures [27] while relieving the user from setting parameter $K_\star$.

III. Accelerating NE

The quadratic time complexity of both single-scale and multiscale NE schemes with respect to N limits their applicability to moderate-sized data sets. This motivated accelerating single-scale methods, by harnessing the typical smallness of the user-defined perplexity $K_\star$ with respect to N. This observation enables defining sparse HD similarities in $\mathcal{O}(N \log N)$ time. The cost functions of single-scale approaches and their gradients can then be estimated using tree-based algorithms [32], [33] or FMMs [34] in $\mathcal{O}(N \log N)$ and $\mathcal{O}(N)$ time respectively. On the other hand, the multiscale framework relies on perplexities covering all data scales. The induced dense HD similarities hinder designing lower complexity multiscale techniques as in the single-scale case. Section III-A focuses on tree-based approximations for SNE and t-SNE, whereas Section III-B details the proposed randomized acceleration

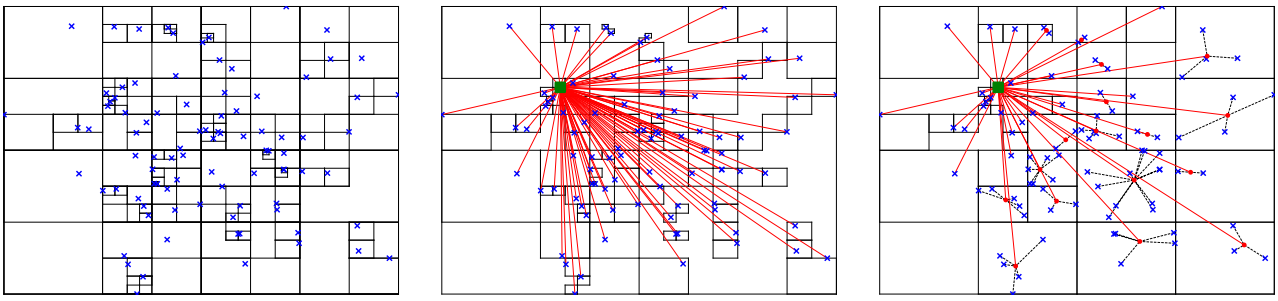

(a) (b) (c)

Fig. 1. (a) Quadtree of a 2-D data set with crosses as data points. (b) Complete pairwise interactions between the square data point and the remaining crosses. (c) BH approximation of the complete pairwise interactions with the square data point, induced by some threshold θ. The centers of mass employed for the approximation are depicted as dots, linked with dotted lines to the crosses belonging to their cells.

of multiscale methods, with $\mathcal{O}\big(N\log^2 N\big)$ time complexity. In Sections III-A and III-B, Euclidean LD distances are assumed to compute the gradients of the cost functions.

A. Fast Single-Scale Methods

Due to its normalized Gaussian nature, $\sigma_{ij\star}$ vanishes as δ_{ij} grows [33]. A sparse approximation of $\sigma_{ij\star}$ then consists in

$$\widetilde{\sigma}_{ij\star} = \begin{cases} \dfrac{\exp\big(-\widetilde{\pi}_{i\star}\delta_{ij}^2/2\big)}{\sum_{k\in\mathcal{I}_{i\star}}\exp\big(-\widetilde{\pi}_{i\star}\delta_{ik}^2/2\big)}, & \text{if } j\in\mathcal{I}_{i\star} \\ 0, & \text{otherwise} \end{cases} \tag{13}$$

with

$$\widetilde{\pi}_{i\star} \text{ s.t. } \log K_\star = -\sum_{j\in\mathcal{I}_{i\star}} \widetilde{\sigma}_{ij\star}\log\widetilde{\sigma}_{ij\star} \tag{14}$$

where $\mathcal{I}_{i\star}$ indexes the $\lfloor 3K_\star\rceil$ nearest neighbors of $\boldsymbol{\xi}_i$ in $\boldsymbol{\Xi}\backslash\{\boldsymbol{\xi}_i\}$ [32]. The number of nearest neighbors of $\boldsymbol{\xi}_i$ to consider should indeed increase with $K_\star$ since the entropy of $\boldsymbol{\sigma}_{i\star}$ at the right-hand side of (3) is monotonically decreasing with $\pi_{i\star}$ when the distances in $\{\delta_{ij}, j\in\mathcal{I}\backslash\{i\}\}$ are not all equal [25]. Therefore, the greater $K_\star$, the smaller $\pi_{i\star}$, the flatter the HD similarities in $\boldsymbol{\sigma}_{i\star}$, and the more nearest neighbors should be accounted for in (13) for the faithfulness of the approximation. The $\lfloor 3K_\star\rceil$ number is suggested in [32] as it yields impressive DR performances and is employed in this work to ease the comparison with state-of-the-art literature results. The nearest neighbor sets are exactly derived by creating a vantage-point tree [37] on $\boldsymbol{\Xi}$ and performing N depth-first searches, each yielding the $\lfloor 3K_\star\rceil$ nearest neighbors of a datum. A sparse estimate for $\tau_{ij\star}$ then develops as $\widetilde{\tau}_{ij\star} = (\widetilde{\sigma}_{ij\star} + \widetilde{\sigma}_{ji\star})/(2N)$. Both matrices $[\widetilde{\sigma}_{ij\star}]_{i,j\in\mathcal{I}}$ and $[\widetilde{\tau}_{ij\star}]_{i,j\in\mathcal{I}}$ have $\mathcal{O}(K_\star N)$ nonzero entries instead of $\mathcal{O}\big(N^2\big)$ for their nonsparse versions. The tree is created in $\mathcal{O}(N\log N)$ time and each search costs $\mathcal{O}(K_\star\log N)$ time, hence providing $\mathcal{I}_{i\star}$ for all $i\in\mathcal{I}$ in $\mathcal{O}(K_\star N\log N)$ time.

Efficiently evaluating the SNE and t-SNE cost functions and their gradients still entails cheaply estimating their remaining nonsparse, LD terms. A BH algorithm [38] can be developed for this purpose, leading to BH SNE [6], [33] and BH t-SNE [32]. The computations are made explicit for the gradient of t-SNE cost function in Appendix A and can be adapted to the SNE case and to estimate the cost functions. Fig. 1 shows the main principles of the BH algorithm. When the LD dimension P is set to 2, a quadtree is first created on the LD embedding in $\mathcal{O}(N)$ time [32], as shown in Fig. 1(a). An octree may similarly be constructed if $P=3$, but the exponential increase of the number of cells limits the suitability of such space-partitioning trees for larger LD dimensions. Then, instead of evaluating exactly all pairwise interactions between the LD points, which is shown in Fig. 1(b), they are approximated for faraway data samples using the centers of mass of the LD coordinates in the cells of the quadtree [33], as shown in Fig. 1(c). While conducting exact computations as in Fig. 1(b) leads to $\mathcal{O}\big(N^2\big)$ time complexity when performed on the entire data set, the BH estimation scheme of Fig. 1(c) runs in $\mathcal{O}(N\log N)$ average time [32]. A threshold hyperparameter $\theta\in[0,1]$ determines when to launch the approximation while traversing the tree and thus balances the speed and the accuracy of the evaluation. Larger θ speeds up computations with rougher approximations. The DR quality of the t-SNE acceleration remains, however, stable under variations of θ [39].

Assuming that $K_\star$ is small compared to N, approximations of $C_{t\star}$ and its gradient are then obtained in $\mathcal{O}(N\log N)$ average time [32] and can be used in gradient-based minimization schemes to tune the LD embeddings of BH t-SNE.

B. Fast Multiscale Methods

A crucial aspect of fast single-scale methods stems from their sparse HD similarities. These rely on nearest neighbor sets $\mathcal{I}_{i\star}$ for each $i\in\mathcal{I}$, with $\big|\mathcal{I}_{i\star}\big| = \lfloor 3K_\star\rceil$. A vantage-point tree [37] computes these sets in $\mathcal{O}(K_\star N\log N)$ time, which reduces to $\mathcal{O}(N\log N)$ if $K_\star \ll N$.

Multiscale methods combine single-scale similarities tuned at several data scales, employing exponentially growing perplexities. In particular, K_H lies in the $\mathcal{O}(N)$ range, leading to neighbor sets $\mathcal{I}_{iH}$ with $\mathcal{O}(N)$ size for each $i\in\mathcal{I}$, since $\big|\mathcal{I}_{iH}\big| = \min(\lfloor 3K_H\rceil, N-1)$. As multiscale HD similarities average the single-scale ones in (10), full multiscale neighbor sets are derived as $\mathcal{I}_i = \cup_{h=1}^{H}\mathcal{I}_{ih} = \mathcal{I}\backslash\{i\}$, to gather the neighbors from all scales. Therefore, the multiscale HD similarity matrix determined by these neighbor sets has $\mathcal{O}\big(N^2\big)$ nonzero entries. This prevents designing sparse multiscale HD similarities as in the single-scale framework.

Single-scale HD similarities with small perplexities excel at modeling local interactions around each data point while reducing the influence of farther away HD objects. They indeed concentrate their probability mass on the nearest neighbors of each datum, which can hence in turn serve

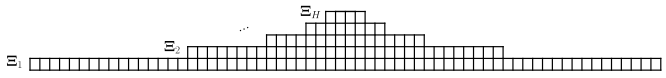

Fig. 2. Hierarchy of HD data sets at all scales. A square refers to an HD sample.

as a remarkable basis to produce sparse approximations. As local structures often rapidly fluctuate, it is in fact crucial to consider the closest neighbors to guarantee the faithfulness of the sparse estimates when processing small scales. On the other hand, single-scale similarities based on large perplexities capture global, large-scale interactions in the data. As these global structures emerge from average trends across important amounts of data points, it is little convincing that their estimation requires exhaustive consideration of all samples. Indeed, while local interactions are short range and induced by very specific sets of neighbors, global ones result from overall consensuses, which can be fairly well approximated using appropriate subsets of data points. In the cost functions of NE methods, evaluating the divergences between probability distributions defined on such subsets may reveal sufficient to relevantly shape the LD embedding according to global HD properties.

However, multiscale similarities combine both types of small and large perplexities, respectively, focusing on local and global HD characteristics. As a consequence, to faithfully accelerate multiscale methods, the design of small and relevant multiscale neighbor sets, denoted by $\widetilde{\mathcal{I}}_i$ for $i \in \mathcal{I}$, entails purposely gathering data points that reasonably model the whole data cloud while at the same time accurately targeting the nearest HD neighbors of each $\boldsymbol{\xi}_i$. The computation of NE cost functions could then be restricted to these subsets $\widetilde{\mathcal{I}}_i$ for each $i \in \mathcal{I}$, which would efficiently score the adequacy of the LD coordinates $\mathbf{x}_i$ in the multiscale spirit, by accounting for both global trends and local interactions in the data.

The hierarchical structure of the multiscale HD similarities, from small to large perplexities, suggests that the set $\widetilde{\mathcal{I}}_i$ should gather data points lying at different ranges of $\boldsymbol{\xi}_i$. Indeed, as small scales require fine levels of details, $\widetilde{\mathcal{I}}_i$ must precisely contain the very close neighbors of $\boldsymbol{\xi}_i$. However, as the scale index increases, only rougher HD characterization is required and a few farther data points from $\boldsymbol{\xi}_i$ can be sampled, providing a higher resolution view. Inspired by this intuition, one can first define a hierarchy $\{\boldsymbol{\Xi}_h\}_{h=1}^H$ of subsampled HD data sets at each scale, where $\boldsymbol{\Xi}_h$ is a random sample of $\boldsymbol{\Xi}$ with $\lfloor 2^{1-h}N \rceil$ elements drawn without replacement. Note that $\boldsymbol{\Xi}_1 = \boldsymbol{\Xi}$. This collection of HD data sets is shown in Fig. 2.

For each $h \in \{1, \ldots, H\}$, a vantage-point tree [37] can be efficiently created on $\boldsymbol{\Xi}_h$ in $\mathcal{O}\big(2^{1-h}N \log(2^{1-h}N)\big)$ time. All the trees are then defined in

$$\mathcal{O}\left(\sum_{h=1}^{H} \frac{N}{2^{h-1}} \log \frac{N}{2^{h-1}}\right) = \mathcal{O}\left(N \log N \sum_{h=1}^{H} \frac{1}{2^h}\right) \quad (15)$$

$$= \mathcal{O}(N \log N) \quad (16)$$

time. The hth tree enables computing the set $\widetilde{\mathcal{I}}_{ih}$ of the $\lfloor 3K_1 \rceil$ nearest neighbors of $\boldsymbol{\xi}_i$ in $\boldsymbol{\Xi}_h \backslash \{\boldsymbol{\xi}_i\}$ in $\mathcal{O}\big(K_1 \log(2^{1-h}N)\big)$ time. The sets $\widetilde{\mathcal{I}}_{ih}$ for all $i \in \mathcal{I}$ and $h \in \{1, \ldots, H\}$ are hence obtained in $\mathcal{O}\big(N \log^2 N\big)$ time, as $K_1 = 2 \ll N$ and as there are $\mathcal{O}(\log N)$ scales. It is worth mentioning that, on average, $\widetilde{\mathcal{I}}_{ih}$ subsamples the set $\mathcal{I}_{ih}$ of the $\lfloor 3K_h \rceil$ nearest neighbors of $\boldsymbol{\xi}_i$ in $\boldsymbol{\Xi} \backslash \{\boldsymbol{\xi}_i\}$, as $\widetilde{\mathcal{I}}_{ih}$ is based on $\boldsymbol{\Xi}_h$ that contains a fraction $2^{1-h} = K_1/K_h$. of $\boldsymbol{\Xi}$.

Defining $\widetilde{\mathcal{I}}_i := \cup_{h=1}^H \widetilde{\mathcal{I}}_{ih}$ then follows the above intuition; the smallest scale is represented by the exact $\lfloor 3K_1 \rceil$ nearest neighbors of $\boldsymbol{\xi}_i$ in $\boldsymbol{\Xi} \backslash \{\boldsymbol{\xi}_i\}$. However, as the scale grows, $\boldsymbol{\Xi}_h$ more and more roughly summarizes $\boldsymbol{\Xi}$ in such a way that the accounted neighbors $\widetilde{\mathcal{I}}_{ih}$ are more and more dispersed in the data cloud in the sake of capturing its global properties.

The sets $\widetilde{\mathcal{I}}_i$ can be employed to define sparse HD similarities focusing on both local and global data relationships. At scale $h \in \{1, \ldots, H\}$, one can establish, for $i, j \in \mathcal{I}$

$$\widetilde{\sigma}_{ijh} = \begin{cases} \dfrac{\exp\big(-\widetilde{\pi}_{ih}\delta_{ij}^2/2\big)}{\sum_{k \in \widetilde{\mathcal{I}}_i} \exp\big(-\widetilde{\pi}_{ih}\delta_{ik}^2/2\big)}, & \text{if } j \in \widetilde{\mathcal{I}}_i \\ 0, & \text{otherwise} \end{cases} \quad (17)$$

with

$$\widetilde{\pi}_{ih} \text{ s.t. } \log K_1 = -\sum_{j \in \widetilde{\mathcal{I}}_{ih}} \widetilde{\sigma}_{ijh}^{\pi} \log \widetilde{\sigma}_{ijh}^{\pi} \quad (18)$$

where

$$\widetilde{\sigma}_{ijh}^{\pi} = \begin{cases} \dfrac{\exp\big(-\widetilde{\pi}_{ih}\delta_{ij}^2/2\big)}{\sum_{k \in \widetilde{\mathcal{I}}_{ih}} \exp\big(-\widetilde{\pi}_{ih}\delta_{ik}^2/2\big)}, & \text{if } j \in \widetilde{\mathcal{I}}_{ih} \\ 0, & \text{otherwise.} \end{cases} \quad (19)$$

Precision $\widetilde{\pi}_{ih}$ is fixed in (18) due to the neighbors $\widetilde{\mathcal{I}}_{ih}$. Sparse multiscale HD similarities then follow as, for $i, j \in \mathcal{I}$:

$$\widetilde{\sigma}_{ij} = H^{-1} \sum_{h=1}^{H} \widetilde{\sigma}_{ijh}, \quad \widetilde{\tau}_{ij} = (\widetilde{\sigma}_{ij} + \widetilde{\sigma}_{ji})/(2N). \quad (20)$$

Their matrices have $\mathcal{O}(N \log N)$ nonzero entries, all derived in $\mathcal{O}\big(N \log^2 N\big)$ total time, as $\big|\widetilde{\mathcal{I}}_i\big|$ scales as $\mathcal{O}(\log N)$.

Sparse multiscale LD similarities could be defined in a similar way. To match them with (20), they should rely on the same sets $\widetilde{\mathcal{I}}_i$ for $i \in \mathcal{I}$, possibly extending each of them with $\mathcal{O}(\log N)$ elements to capture the local and global properties of the LDS. These $\mathcal{O}(\log N)$ additional elements should be iteratively adapted according to the LD embedding modification after each optimization step. Nevertheless, experiments revealed that minimizing the divergence between (20) and such LD similarities leads to LD crushing phenomena, meaning that LD coordinates are overlapping. Indeed, the size of each set $\widetilde{\mathcal{I}}_i$ for $i \in \mathcal{I}$ remains limited to $\mathcal{O}(\log N)$, whether adding the abovementioned $\mathcal{O}(\log N)$ elements or not. Therefore, it is likely that $\widetilde{\mathcal{I}}_k \cap \widetilde{\mathcal{I}}_l = \emptyset$ for $k, l \in \mathcal{I}$. In this case, LD similarities based on the sets $\widetilde{\mathcal{I}}_k$ and $\widetilde{\mathcal{I}}_l$ would make the LD coordinates $\mathbf{x}_k$ and $\mathbf{x}_l$ independent one to another. The lack of LD repulsive forces between them hence enables their LD superposition. Extending this reasoning to a potentially very large number of data point pairs leads to crushed LD embeddings, with poor HD neighborhood preservation. On the other hand, LD interactions can be efficiently estimated with inspiration from the single-scale setting. This motivates defining hybrid cost functions for fast versions of multiscale SNE and t-SNE as

$$\widetilde{C} = -\sum_{i \in \mathcal{I}, j \in \mathcal{I} \backslash \{i\}} \widetilde{\sigma}_{ij} \log s_{ij} \quad (21)$$

TABLE I
TIME COMPLEXITIES OF THE NE SCHEMES FROM SECTIONS II AND III

DR method	Time complexity	
	HD similarities computation at initialization	Iterations in gradient-based optimization
SNE, t-SNE	$\mathcal{O}\left(N^2\right)$	$\mathcal{O}\left(N^2\right)$
BH SNE, BH t-SNE	$\mathcal{O}\left(N \log N\right)$	$\mathcal{O}\left(N \log N\right)$
Multi-scale SNE	$\mathcal{O}\left(N^2 \log N\right)$	$\mathcal{O}\left(N^2 \log N\right)$
Fast Multi-scale SNE	$\mathcal{O}\left(N \log^2 N\right)$	$\mathcal{O}\left(N \log^2 N\right)$
Multi-scale t-SNE	$\mathcal{O}\left(N^2 \log N\right)$	$\mathcal{O}\left(N^2\right)$
Fast Multi-scale t-SNE	$\mathcal{O}\left(N \log^2 N\right)$	$\mathcal{O}\left(N \log N\right)$

and

$$\widetilde{C}_{\mathrm{t}} = -\sum_{i \in \mathcal{I},\, j \in \mathcal{I}\backslash\{i\}} \widetilde{\tau}_{ij} \log t_{ij} \tag{22}$$

which quantify the mismatch between the sparse multiscale HD similarities (20) and the LD ones of genuine multiscale SNE and t-SNE. In (21) and (22), the HD similarities are normalized only through the data points in $\widetilde{\mathcal{I}}_i$ for $i \in \mathcal{I}$, whereas all samples are involved in the LD similarity normalization. Matching these HD and LD similarities then decreases the amplitude of the additional terms in the denominators of the LD similarities, favoring LD spreading, i.e., the tendency to expand the LDS, reported as beneficial to DR quality [13].

After computing (20), a BH algorithm [38] is adapted from Appendix A to estimate (22) as well as its gradient in $\mathcal{O}(N \log N)$ average time. As to (21) and its gradient, we develop their BH approximation in $\mathcal{O}\left(N \log^2 N\right)$ average time. It is detailed in Appendix B for the gradient of (21), from which the BH estimation of (21) itself can be easily derived. As presented in Appendix B, it is noteworthy that the BH estimation of the gradient of (21) entails two tree traversals instead of one for the BH approximation of (22) and its gradient. One can thus expect an increased sensitivity of the multiscale SNE acceleration with respect to the BH threshold θ, compared to fast single-scale and multiscale t-SNE, since the estimation quality of the first traversal affects the second one.

The overall time complexity of the presented fast multiscale schemes evolves as $\mathcal{O}\left(N \log^2 N\right)$, importantly without quadratic dependence with N. Note that in fast multiscale t-SNE, although determining the HD similarities (20) takes $\mathcal{O}\left(N \log^2 N\right)$ time once at initialization, only $\mathcal{O}(N \log N)$ average time is required to approximate the gradient of (22), which is iteratively performed in gradient-based optimization. This is emphasized in Table I, which gathers the time complexities of the NE algorithms from Sections II and III.

It is noteworthy that $j \in \widetilde{\mathcal{I}}_i$ does not imply $i \in \widetilde{\mathcal{I}}_j$. One may easily extend the multiscale neighbor sets to ensure this property, but experiments revealed that it does not influence the performances much; only tiny improvements in terms of DR quality were observed, at the expense of slightly increased computation times. As multiscale t-SNE is defined through symmetric similarities, its fast version extends the sets $\widetilde{\mathcal{I}}_i$ to ensure the above property, but not fast multiscale SNE.

The proposed accelerations are based on the definition of multiscale neighbor sets $\widetilde{\mathcal{I}}_i \subset \mathcal{I}\backslash\{i\}$ for all $i \in \mathcal{I}$, with a limited number of elements emulating the intrinsic hierarchy of the data scales. Indeed, $\widetilde{\mathcal{I}}_i$ gathers the closest neighbors of $\boldsymbol{\xi}_i$ as well as farther away HD samples, more diffused in the data cloud. This enables accurately describing the local, quickly fluctuating properties around $\boldsymbol{\xi}_i$ while providing a succinct, higher order summary of the global HD characteristics. The induced sparse multiscale HD similarities (20) hence model data proximities at different ranges, unlike their single-scale counterparts (13). An additional $\mathcal{O}(\log N)$ factor arises in the time complexity with respect to fast single-scale approaches, with minor impact compared to the linear dependence in N. Matching the HD similarities (20) with BH estimates of the multiscale LD similarities enables efficiently mapping both local and global HD structures in the LDS while avoiding LD crushing. Similar to multiscale SNE and t-SNE, multiscale NeRV and JSE can be accelerated due to the multiscale neighbor sets along with BH approximations.

IV. EXPERIMENTAL RESULTS

The performances of the presented fast multiscale methods are studied in the context of two main experiments, in terms of both DR quality and computation time. First, Section IV-A considers several moderate-sized databases, with a few thousands of samples each, which enables applying the original, nonaccelerated versions of the algorithms for comparison purposes. The assessed methods are hence multiscale SNE (Ms SNE), multiscale t-SNE (Ms t-SNE), and their proposed accelerations (FMs SNE and FMs t-SNE). For the sake of comparison, the results of the single-scale t-SNE and its BH version (BH t-SNE), detailed in Sections II-A and III-A, are also discussed. The behavior of the fast methods with respect to the BH threshold θ is analyzed to suggest adequate values suitable across multiple databases. Second, Section IV-B deals with large-scale data sets, with tens or hundreds of thousands samples each. The quadratic time complexity of the nonaccelerated schemes prevents their application on these databases. Therefore, only scalability of the fast schemes is tested in this setting.

In Section IV-A and IV-B, HD and LD distances are Euclidean and 2-D embeddings are targeted ($P = 2$), as typically desired in exploratory visualization. On each database, both fast multiscale algorithms are applied 30 times, each with different random subsamplings of the HD data set. Average results are then reported over these replications, along with standard deviations. Moreover, due to the repetitions, statistical tests allow evaluating the significance of the difference in average performances of the methods. Paired tests are computed when FMs SNE and FMs t-SNE are confronted with each other and one-sample tests for the mean otherwise. For each studied score, if their 30 values for each fast multiscale method are normally distributed according to D'Agostino and Pearson's omnibus normality test [40], two-tailed t-tests are employed, and Wilcoxon tests otherwise. The test significance level is fixed to $\alpha = 0.05$. As multiple hypothesis tests result from each database analysis, the Holm–Bonferroni correction is used [41]. Nonsignificant differences are hence considered as statistically significant with probability bounded by α.

The compared single-scale and multiscale algorithms are optimized as advised in their respective

papers [13], [27], [32], the proposed fast multiscale methods being minimized as their nonfast versions. In particular for the latter, K_1 and H are, respectively, set to 2 and $\lfloor \log_2(N/K_1) \rceil$, multiscale optimization [27] is executed and the limited-memory Broyden–Fletcher–Goldfarb–Shanno (L-BFGS), algorithm is employed [42]. As to single-scale t-SNE and BH t-SNE, momentum gradient descent is used along with early exageration, with parameters as described in [13] and [32]. The perplexity $K_\star$ is set to 50, as in [32]. In both single-scale and multiscale settings, the iterations of the optimization schemes are stopped as soon as the gradient infinite norm is below 10^{-5} or the cost function relative updates are bounded by 10^{-8} or a maximum number is reached. The latter maximum number must, however, be carefully defined as different data sets require, obviously, different numbers of iterations before convergence of the LD embedding. Comparing converged and nonconverged results of the methods across databases may likely lead to misleading conclusions on the behavior of the algorithms, in terms of both achievable DR quality and computation time. On the other hand, large numbers of samples often require unaffordable amounts of time before reaching convergence of the optimization. For these reasons, the number of iterations of optimization algorithms is limited to 10^5 in Section IV-A. As much fewer iterations are typically required for convergence, this threshold is almost equivalent to an unbounded number of iterations. Thus, in Section IV-A, the optimization schemes terminate according to the first two above conditions, on the gradient norm and relative cost function updates. This ensures comparability of the performances across data sets while maintaining affordable computation times since moderate-sized databases are tackled. As to Section IV-B, since huge numbers of samples are considered, the maximum number of iterations is reduced to avoid dealing with too long computation times, as one would proceed in a practical context when facing large-scale databases. For BH t-SNE, 10^3 iterations are performed, as suggested in [32]. For FMs SNE and FMs t-SNE, as few as 30 iterations per L-BFGS run are at most executed. All simulations and computation times were obtained due to a desktop computer with a 4-core Intel Xeon CPU E3-1245 v5 at 3.5 GHz, with 32-GB RAM.

A. Comparison Between Fast and Nonaccelerated Methods

The data sets studied in this section originate from the UCI Machine Learning Repository [43]: Anuran calls MFCCs (Anuran), Combined cycle power plant (Plant) [44], [45], Musk version 2 (Musk), Spambase, Gesture phase segmentation (Gesture) [46], Statlog landsat satellite (Satellite), First-order theorem proving (Theorem) [47], Waveform database generator version 2 (Waveform), Isolet, Madelon [48], and Abalone and Wine quality (Wine) [49]. Their numbers N and M of samples and features are shown in Table II.

DR quality is usually related to the HD neighborhood preservation in the LDS [17], [50], [51]. It is evaluated due to criteria [12], computed in $\mathcal{O}\left(N^2 \log N\right)$ time. The K nearest neighbors of $\boldsymbol{\xi}_i$ and $\mathbf{x}_i$ can first be denoted as ν_i^K and n_i^K, respectively, in the HDS and LDS. The average normalized agreement of these $K-$ary neighborhoods develops as

$$Q_{\mathrm{NX}}(K) = \frac{1}{N} \sum_{i \in \mathcal{I}} \frac{\left| \nu_i^K \cap n_i^K \right|}{K} \in [0, 1]. \tag{23}$$

Since random LD points yield $\mathbb{E}[Q_{\mathrm{NX}}(K)] = K/(N-1)$

$$R_{\mathrm{NX}}(K) = \frac{(N-1)Q_{\mathrm{NX}}(K) - K}{N-1-K} \tag{24}$$

enables comparing varying neighborhood sizes [21]. As prevailing neighborhoods are typically local, a log scale for K is used to display $R_{\mathrm{NX}}(K)$, whose resulting area under the curve (AUC)

$$\mathrm{AUC} = \left(\sum_{K=1}^{N-2} K^{-1} \right)^{-1} \cdot \sum_{K=1}^{N-2} \frac{R_{\mathrm{NX}}(K)}{K} \in [-1, 1] \tag{25}$$

grows with DR quality. The latter is hence characterized by accounting for all scales, with a focus on smaller ones [27].

Fig. 3 presents the results as a function of the BH threshold θ on Anuran, Plant, Musk, Spambase, and Gesture.

1) Nonfast Methods: On all databases, Ms SNE is consistently the best method in terms of AUC, at the expense of long computation times. Indeed, multiscale HD and LD similarities enable very accurate tuning of the LDS, with high resolution as they involve both large and small precisions. Nevertheless, the induced LD Gaussian neighborhoods likely rapidly locally fluctuate, making the gradient of Ms SNE sensitive to small LD variations. Its bad scaling hence causes a slow convergence of the optimization process. Next, the AUC of Ms t-SNE is always second to Ms SNE, except on some databases when small BH thresholds are employed with FMs SNE and on Spambase, on which FMs t-SNE performs better. In any case, Ms SNE and Ms t-SNE systematically outperform single-scale t-SNE and BH t-SNE in terms of DR quality. From the running time perspective, Ms t-SNE is much more affordable than Ms SNE. The heavy-tailed Student t-distributed LD similarities likely induce a more stable gradient regarding LD variations. Ms t-SNE is even faster than single-scale t-SNE. Although the comparison is less straightforward in this last case since Ms t-SNE and single-scale t-SNE rely on different optimization schemes, one may argue that accounting for global properties in Ms t-SNE further constrains the LDS structure, facilitating the cost function minimization. On the other hand, as t-SNE focuses on local aspects, the global LDS organization is left undetermined. Shaping it hence probably requires additional time to fix these degrees of freedom.

2) Fast Methods: The AUC of BH t-SNE is stable with respect to the BH threshold θ, in agreement with the results mentioned in [39]. The same remarkable behavior is preserved in FMs t-SNE, which is consistently and statistically significantly above BH t-SNE and t-SNE. FMs SNE is, however, much more sensitive to the BH threshold: its average AUC quickly drops with θ, with increasing standard deviation as the threshold increases. This is due to the two successive tree traversals involved in the FMs SNE gradient approximation: as the second traversal employs the results of the first one, augmenting that θ not only affects the estimation quality of the first pass but also more severely deteriorates the accuracy of the second one, in a cascading effect. The DR quality of FMs SNE thus rapidly decreases

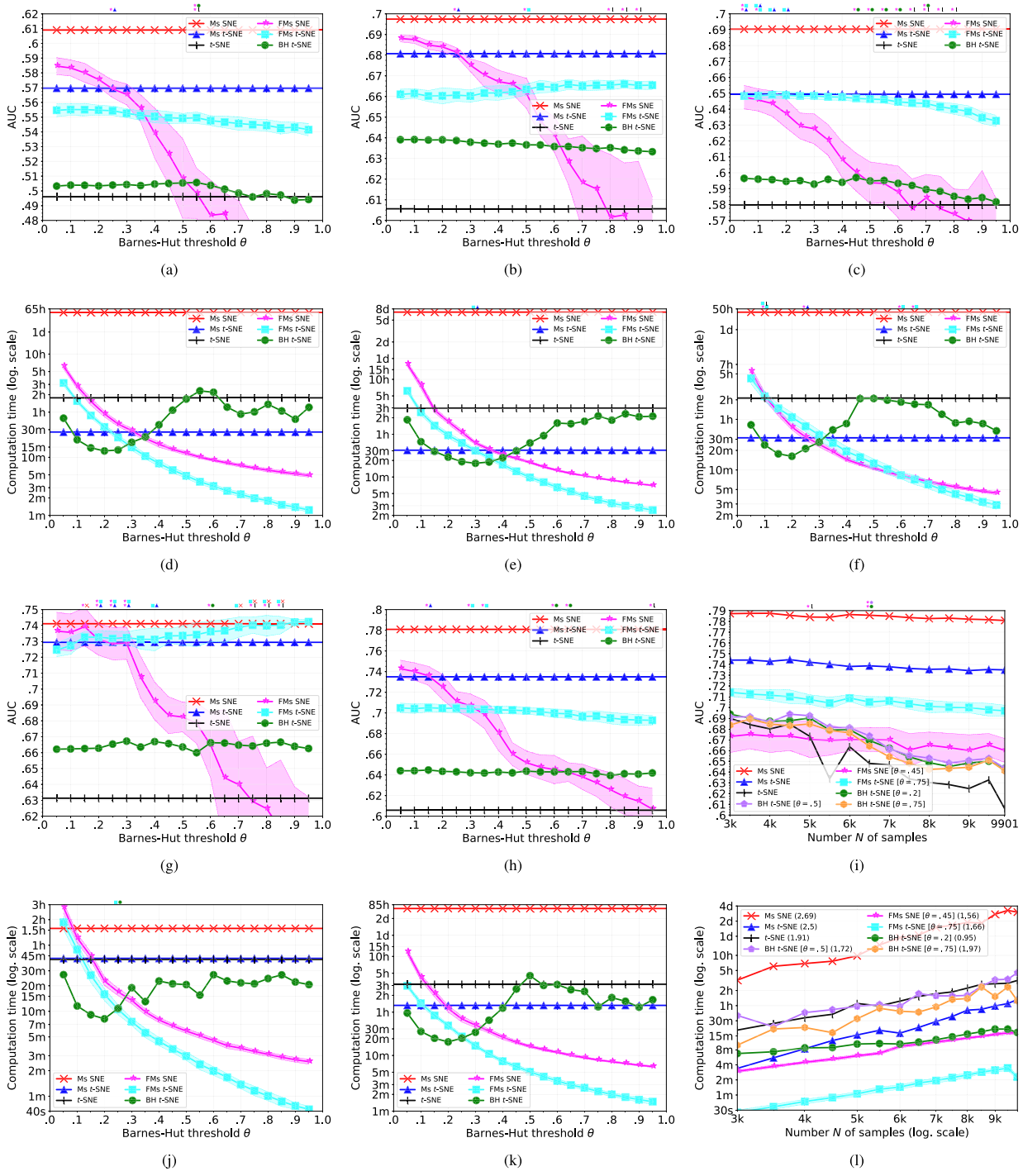

Fig. 3. (a) AUC of the DR methods on Anuran as a function of the BH threshold θ, from 0.05 to 0.95 with 0.05 step. Average performances over 30 random subsamplings are depicted for FMs SNE and FMs t-SNE, with shaded areas delimiting one standard deviation around the mean. Above the figure, pairs of markers indicate schemes that are not statistically significantly different, for instance, Ms t-SNE and FMs SNE for $\theta = 0.25$. (b), (c), (g), and (h) Similar to (a) but, respectively, on Plant, Musk, Spambase, and Gesture, respectively. (d)–(f), (j), and (k) Analogous to (a)–(c), (g), and (h), but for the computation time. Log scale is used for the y-axis and s, m, h, and d refer to second, minute, hour, and day. (i) Similar to (h) but for subsamples of the Gesture data set, with fixed BH thresholds θ described in the legend. The number N of samples varies with steps of 500 on the x-axis. (l) Analogous to (i) but for the computation time, on the y-axis. Both axes are in log scale. For each DR algorithm, the slope of a linear regression of its results in log–log scale is provided in parentheses in the legend.

with θ, while small BH thresholds yield high AUC since, in this case, both tree traversals deliver precise approximations. Smaller θ nevertheless induces larger running times for both FMs SNE and FMs t-SNE. Considering the AUC and computation time dependence of FMs SNE with respect to θ, its BH threshold should be carefully determined to ensure a proper balance between DR quality and running time. For this reason, a threshold $\theta = 0.45$ is considered for FMs SNE in the remaining experiments. On the other hand, FMs t-SNE can accommodate with larger BH thresholds

due to its AUC dependence with θ, enabling to decrease computation time without suffering from significant loss in DR quality. As it can reach high DR quality with low computation time much more easily and as it is intrinsically faster since entailing only one tree traversal per gradient estimation instead of two, one can state that FMs t-SNE is superior to FMs SNE. For the subsequent experiments, $\theta = 0.75$ is used with FMs t-SNE. Noticeably, although both FMs SNE and FMs t-SNE get, as expected, faster as θ increases, BH t-SNE behaves differently. Indeed, on all data sets, the running time of BH t-SNE first decreases with θ, reaches a minimum at around $\theta = 0.2$, and then increases before remaining roughly stable. This intriguing phenomenon may be explained as larger θ accelerates each gradient estimation but also induces coarser approximations. These likely result in more iterations before reaching convergence of the momentum gradient descent. The L-BFGS scheme employed in FMs methods less suffers from these rougher estimations, probably due to the successive Hessian approximations it computes, which partly cancel the influence of noisy gradient estimates. Therefore, for most BH thresholds, FMs t-SNE is statistically significantly faster than BH t-SNE. For completeness of the comparison, three thresholds are further employed with BH t-SNE, namely, 0.2 as it minimizes running times on Anuran, Musk, Spambase, Gesture, and almost Plant, 0.5 as in [32], and 0.75 as larger value.

Fig. 3(i) and (l) shows the AUC and running time of the methods as a function of the number of points in subsamples of Gesture, respectively. In terms of AUC, Ms SNE remains the best method, followed by Ms t-SNE and then FMs t-SNE. The last three methods are close, smaller data sets favoring BH t-SNE and FMs SNE being superior on larger ones. Smaller BH thresholds would improve the accuracy of FMs SNE on smaller subsamples. As to the computation times, FMs t-SNE is consistently and statistically significantly the fastest method, which raises the interest for it in light of its AUC performances. FMs SNE is second and BH t-SNE is indeed faster with $\theta = 0.2$. Using the log–log axes as in Fig. 3(l), the slope of linear regressions of the method timings should reveal their time complexity. One would expect a slope near 2 for t-SNE, above 2 for Ms SNE and Ms t-SNE, above 1 for BH t-SNE and higher than 1 for FMs SNE and FMs t-SNE, as these methods, respectively, have $\mathcal{O}(N^2)$, $\mathcal{O}(N^2 \log N)$, $\mathcal{O}(N \log N)$, and $\mathcal{O}(N \log^2 N)$ theoretical time complexity. Such slopes are indeed experimentally observed (larger numbers of samples would obviously yield more accurate values at the expense of much larger running times for nonfast methods).

Table II provides performances of the methods on all databases using specific BH thresholds. Ms SNE keeps the best AUC and slowest computation times. With more affordable running times, Ms t-SNE is always second in AUC except on Spambase on which FMs t-SNE is superior. Ms t-SNE is also faster than t-SNE, except on Spambase and Madelon. FMs t-SNE is consistently and statistically significantly the fastest method and yields the highest AUC among accelerated schemes, except on Plant and Satellite, on which FMs SNE is superior, without statistical significance on Plant, and on Isolet, on which BH t-SNE performs well, without being statistically different from FMs SNE in AUC. FMs t-SNE also statistically significantly beats t-SNE in terms of AUC, except on Waveform and Madelon. The computation time of BH t-SNE is indeed minimized with $\theta = 0.2$, except on Waveform on which $\theta = 0.5$ is slightly faster. FMs SNE is not as fast as FMs t-SNE but still generally results in statistically significantly larger AUC than t-SNE and BH t-SNE, in less or similar time as BH t-SNE and less time than t-SNE and Ms t-SNE. The AUC difference between Ms SNE and FMs SNE is always greater than between Ms t-SNE and FMs t-SNE, probably due to the two tree traversals required for the gradient estimation.

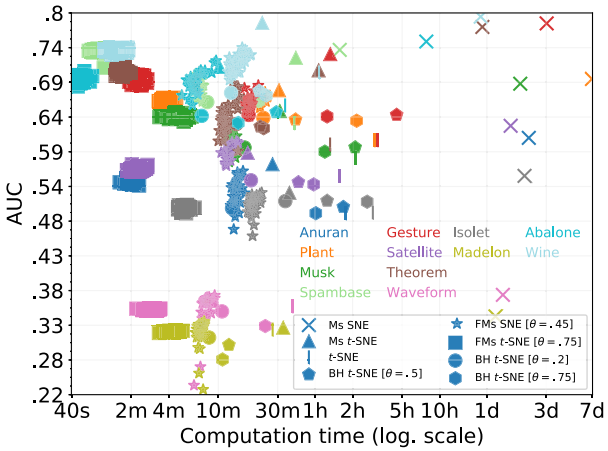

Fig. 4. AUC of the DR methods on moderate-sized data sets as a function of their computation time in log-scale, with s, m, h, and d referring to second, minute, hour, and day. Results of FMs SNE and FMs t-SNE are depicted for 30 different random subsamplings. The markers and colors, respectively, differentiate the DR methods and data sets. The data sets names are indicated using their associated colors to enable their identification. Contrasts best viewed using colors.

Fig. 4 shows the results given in Table II. The high concentration of FMs t-SNE markers in the top-left part of the figure highlights its superiority with respect to the other DR schemes. The performances of FMs SNE and FMs t-SNE are reported for 30 different random subsamplings, and one can visually observe the variability of their performances. While FMs SNE is stable in terms of computation time but slightly less in AUC for reasons detailed below, FMs t-SNE is remarkably consistent across the random subsamplings. All conclusions drawn from Table II are shown in Fig. 4.

Fig. 5 shows $R_{\mathrm{NX}}(K)$ curves for Anuran, Musk, and Satellite. Both original and accelerated multiscale methods outperform single-scale algorithms in terms of local and global neighborhood preservation. Single-scale schemes are only close or slightly above for neighborhood sizes near the perplexity. Indeed, as mentioned in [27], at the expense of a small loss around the perplexity, the multiscale behavior uplifts the curve for all other neighborhood sizes. FMs SNE is close to Ms SNE in terms of global neighborhood preservation but does not reproduce local ones as well. FMs t-SNE behaves oppositely when compared to Ms t-SNE.

It is noteworthy that in Fig. 3, Table II, and Figs. 4 and 5, the standard deviations of FMs SNE are systematically larger than for FMs t-SNE. This indicates that FMs SNE is more sensitive to the random subsamplings than FMs t-SNE, yielding magnified variations of the small neighborhood preservation in Fig. 5. This increased sensitivity likely results from the

TABLE II

PERFORMANCES OF THE DR METHODS ON MODERATE-SIZED DATA SETS, IN TERMS OF AUC AND OF COMPUTATION TIME IN SECONDS. FOR FMS SNE AND FMS t-SNE, THE PROVIDED RESULTS ARE AVERAGES OVER 30 RANDOM SUBSAMPLINGS, WITH STANDARD DEVIATIONS IN PARENTHESES. IN EACH ROW, THE GREATEST AUC OR SMALLEST TIME IS INDICATED IN BOLD, AND AN ASTERIX HIGHLIGHTS THE HIGHEST AUC AMONG THE FAST SCHEMES. RESULTS ARE IN ITALIC (RESP. UNDERLINED) WHEN NOT STATISTICALLY SIGNIFICANTLY DIFFERENT FROM FMS SNE (RESP. FMS t-SNE)

		Ms SNE	FMs SNE $\theta = 0.45$	Ms t-SNE	FMs t-SNE $\theta = 0.75$	t-SNE	BH t-SNE $\theta = 0.2$	BH t-SNE $\theta = 0.5$	BH t-SNE $\theta = 0.75$
Anuran $N = 7195$ $M = 22$	AUC [%]	**60.905**	52.506 (2.047)	56.966	54.495 (0.388)*	49.605	50.341	50.543	49.592
	Time [s]	187629	822 (55)	1637	**119** (**9**)	6352	773	6064	3645
Plant $N = 9568$ $M = 5$	AUC [%]	**69.743**	66.602 (0.474)*	68.072	*66.545* (*0.244*)	60.563	63.901	63.658	63.476
	Time [s]	603853	1315 (69)	1845	**231** (**20**)	10783	1381	2503	7760
Musk $N = 6598$ $M = 166$	AUC [%]	**69.033**	60.042 (1.191)	64.941	64.148 (0.299)*	57.973	59.453	59.484	58.835
	Time [s]	160163	736 (39)	1873	**299** (**40**)	7660	974	7546	4310
Spambase $N = 4601$ $M = 57$	AUC [%]	**74.11**	68.352 (1.157)	72.942	74.019 (0.508)*	63.132	66.281	66.355	66.417
	Time [s]	5675	404 (25)	2519	**70** (**9**)	2442	489	1238	1267
Gesture $N = 9901$ $M = 18$	AUC [%]	**78.084**	66.011 (1.102)	73.493	69.693 (0.518)*	60.581	64.345	64.367	64.119
	Time [s]	261167	1035 (63)	4761	**136** (**12**)	11412	1052	16263	4492
Satellite $N = 6435$ $M = 36$	AUC [%]	**62.715**	58.617 (1.036)*	*58.672*	56.269 (0.264)	55.238	54.538	54.258	53.916
	Time [s]	134074	718 (49)	1034	**138** (**14**)	5698	1098	2641	3506
Theorem $N = 6118$ $M = 53$	AUC [%]	**77.553**	63.577 (2.302)	71.056	71.031 (0.459)*	59.935	*62.987*	*62.601*	62.347
	Time [s]	79442	686 (79)	3840	**101** (**6**)	4747	839	1304	1388
Waveform $N = 5000$ $M = 40$	AUC [%]	**37.343**	34.885 (3.052)	36.444	*35.136* (*0.09*)*	*35.625*	*34.861*	*34.02*	32.656
	Time [s]	116158	467 (37)	547	**176** (**17**)	2366	643	*469*	1431
Isolet $N = 7797$ $M = 617$	AUC [%]	**55.203**	50.711 (1.438)	52.684	*50.333* (*0.333*)	49.71	*51.408*	*51.469**	*51.318*
	Time [s]	173318	1118 (79)	2236	**328** (**25**)	10473	2073	4494	9424
Madelon $N = 4400$ $M = 500$	AUC [%]	**34.112**	31.367 (2.213)	*32.442*	*31.832* (*0.083*)*	*32.155*	*30.934*	29.834	27.637
	Time [s]	101184	420 (20)	1993	**255** (**25**)	1640	506	730	648
Abalone $N = 4177$ $M = 7$	AUC [%]	**75.36**	69.299 (1.509)	71.576	*69.809* (*0.46*)*	65.798	64.207	64.749	63.146
	Time [s]	28163	395 (60)	613	**47** (**4**)	2065	441	1751	867
Wine $N = 6497$ $M = 11$	AUC [%]	**79.093**	71.949 (1.31)	78.184	74.071 (0.237)*	70.731	67.665	67.954	67.261
	Time [s]	77021	847 (105)	1353	**93** (**12**)	3868	759	1280	1457

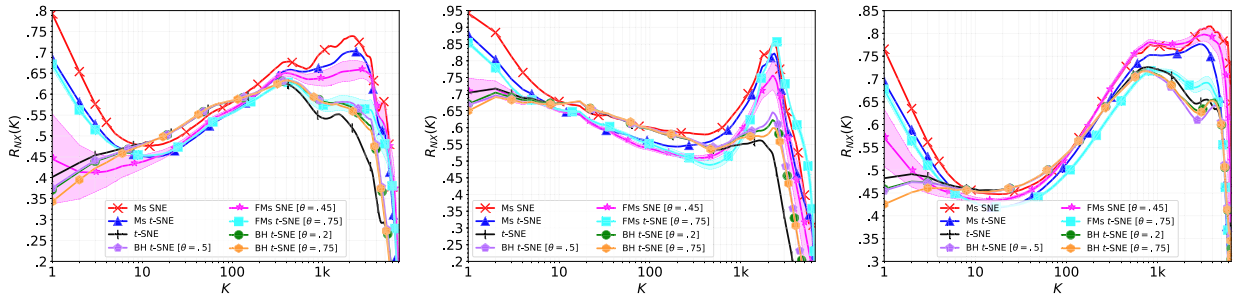

(a) (b) (c)

Fig. 5. (a) $R_{NX}(K)$ curves of the DR methods on Anuran as a function of the neighborhood size K, using the same BH thresholds as in Table II. Average curves over 30 random subsamplings are shown for FMs SNE and FMs t-SNE, with shaded areas delimiting one standard deviation around the mean, as in Fig. 3. A log scale is employed for the neighborhood size K. (b) and (c) Similar but, respectively, on Musk and Satellite.

two tree traversals of the FMs SNE gradient estimation. Indeed, the BH algorithm is directly dependent on the LD configuration, which is itself related to the considered HD data subsampling. The larger influence of the BH algorithm on FMs SNE than on FMs t-SNE, caused by the two tree passes performed per data point at each iteration, then induces an increased sensitivity of FMs SNE with respect to the HD data subsamplings.

B. Scalability Analysis of the Fast Methods

Nonaccelerated NE schemes can manage up to a few thousand samples, due to their quadratic time complexity. Fast methods better scale on large data sets, with tens or hundreds of thousands samples. This section hence studies their performances in this last context, using data sets from the UCI Machine Learning Repository [43]: Statlog Shuttle (Shuttle), Sensorless Drive Diagnosis (Sensorless), SGEMM

TABLE III

PERFORMANCES OF THE FAST DR METHODS ON LARGE-SCALE DATA SETS, IN TERMS OF $\overline{\text{AUC}}$ AND OF COMPUTATION TIME IN SECONDS. FOR FMS SNE AND FMS t-SNE, THE PROVIDED RESULTS ARE AVERAGES OVER 30 RANDOM SUBSAMPLINGS, WITH STANDARD DEVIATIONS IN PARENTHESES. IN EACH ROW, THE GREATEST $\overline{\text{AUC}}$ OR SMALLEST TIME IS INDICATED IN BOLD. RESULTS ARE IN ITALIC (RESP. UNDERLINED) WHEN NOT STATISTICALLY SIGNIFICANTLY DIFFERENT FROM FMS SNE (RESP. FMS t-SNE)

		FMs SNE $\theta = 0.45$	FMs t-SNE $\theta = 0.75$	BH t-SNE $\theta = 0.2$	BH t-SNE $\theta = 0.5$	BH t-SNE $\theta = 0.75$
Shuttle $N = 58000$ $M = 9$	$\overline{\text{AUC}}$ [%]	**57.684 (0.716)**	54.009 (0.35)	50.404	50.448	50.396
	Time [s]	33448 (3732)	**1146 (26)**	5610	2234	1725
Sensorless $N = 58509$ $M = 48$	$\overline{\text{AUC}}$ [%]	**43.996 (0.576)**	*43.945 (0.593)*	38.934	38.91	38.74
	Time [s]	17790 (1257)	**550 (21)**	6350	2316	1745
Sgemm $N = 241600$ $M = 18$	$\overline{\text{AUC}}$ [%]	–	**59.022 (0.057)**	12.277	12.277	12.277
	Time [s]	–	11812 (254)	3946	1144	**805**
Covertype $N = 581012$ $M = 54$	$\overline{\text{AUC}}$ [%]	–	**42.556 (0.104)**	0.756	0.756	0.756
	Time [s]	–	7083 (151)	11813	3354	**2277**
Gas $N = 928991$ $M = 11$	$\overline{\text{AUC}}$ [%]	–	**49.559 (9.218)**	5.283	5.283	5.283
	Time [s]	–	16449 (1664)	16835	4719	**3171**

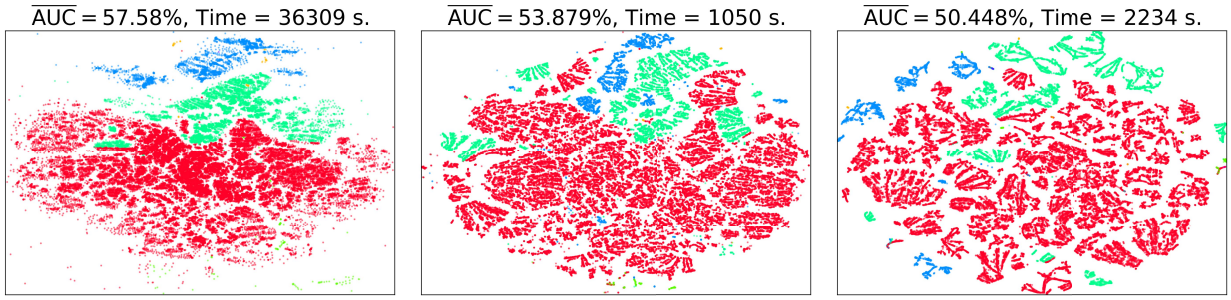

(a) (b) (c)

Fig. 6. (a) 2-D embedding of Shuttle obtained by one of the 30 applications of FMs SNE ($\theta = 0.45$). The classes in the data set are depicted using different colors. The computation time provided in the title of the figure is in seconds. (b) and (c) Similar but for FMs t-SNE ($\theta = 0.75$) and BH t-SNE ($\theta = 0.5$). The embedding of BH t-SNE is displayed with $\theta = 0.5$ as it maximizes its $\overline{\text{AUC}}$ on Shuttle among $\{0.2, 0.5, 0.75\}$ in Table III.

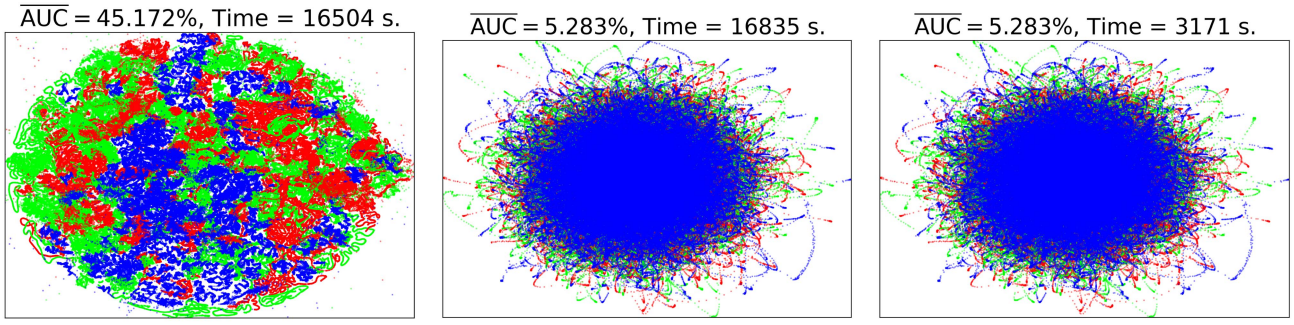

(a) (b) (c)

Fig. 7. (a) 2-D embedding of Gas obtained by one of the 30 applications of FMs t-SNE ($\theta = 0.75$). The classes in the data set are depicted using different colors. The computation time provided in the title of the figure is in seconds. (b) and (c) Similar but for BH t-SNE, respectively, with $\theta = 0.2$ and $\theta = 0.75$.

GPU kernel performance (Sgemm) [52], and Covertype and Gas sensors for home activity monitoring (Gas) [53]. Table III shows their numbers N and M of samples and features.

To assess DR quality, the AUC is no longer suitable as its evaluation requires $\mathcal{O}(N^2 \log N)$ time. Nevertheless, the start of the $R_{\text{NX}}(K)$ curve, with K ranging from 1 to $\overline{K}$, can be computed in $\mathcal{O}(\overline{K} N \log N)$ time, thanks to vantage-point trees. The area $\overline{\text{AUC}}$ of this reduced curve develops as (25), but with the upper limits of the sums replaced with $\overline{K}$. The smaller $\overline{K}$ compared to N, the more the $\overline{\text{AUC}}$ focuses on local neighborhoods compared to AUC. In this section, $\overline{K}$ is set to 10^4, to consider similar neighborhood sizes as in Section IV-A.

Table III gathers the results. On Shuttle and Sensorless, both with tens of thousands samples, FMs SNE performs best in terms of $\overline{\text{AUC}}$, but with the largest computation times. This is due to the $\mathcal{O}(N \log^2 N)$ time complexity of each gradient

estimation, moreover involving two tree traversals per data point, whereas the optimization iterations in BH t-SNE and FMs t-SNE only cost $\mathcal{O}(N \log N)$ time, with a single tree pass per sample. FMs t-SNE is statistically significantly the fastest scheme, also with statistically significantly greater $\overline{\text{AUC}}$ than BH t-SNE. It is noteworthy that increasing θ decreases the running time of BH t-SNE, differently to what is observed in Section IV-A. Indeed, computing 10^3 momentum gradient descent steps does not guarantee LDS convergence. Therefore, larger BH thresholds may accelerate BH t-SNE optimization when stopped after 10^3 iterations, as increasing θ yields cheaper BH estimates and faster iteration evaluations.

Fig. 6 shows the 2-D embeddings of Shuttle as computed by FMs SNE, FMs t-SNE, and BH t-SNE. This database contains unbalanced labels, 80% of its samples belonging to a single class. Visually, both fast multiscale methods tend to more regroup the classes than BH t-SNE. Fig. 6(c) moreover presents cluster overemphasis produced by BH t-SNE, which affects its $\overline{\text{AUC}}$ with respect to FMs SNE and FMs t-SNE. Indeed, although matching Gaussian similarities with heavy-tailed Student t ones is motivated by the crowding problem to compensate for the relative loss of volume from the HDS to the LDS [13], it typically introduces artificial clusters in the embedding since midrange to distant neighbors are further repelled [28]. In Fig. 6(b), FMs t-SNE is also subject to this phenomenon but to a lesser extent, as multiple Gaussian functions with increasing tails are averaged in the HDS, reducing the gap with the heavy-tailed Student t distribution. In contrast, as suggested in Fig. 6(a) and its dominant $\overline{\text{AUC}}$, FMs SNE is more robust to cluster overemphasis, due to the multiscale Gaussian similarities it employs in both spaces.

As to Sgemm, Covertype, and Gas, the results of FMs SNE with $\theta = 0.45$ are not reported in Table III as these databases contain hundreds of thousands samples, inducing intractable computation times when applying the method with 30 different random subsamplings. Larger thresholds could have been employed, but they yield unstable DR quality, as suggested in Fig. 3. Although BH t-SNE is the fastest scheme, FMs t-SNE impressively outperforms it in terms of $\overline{\text{AUC}}$. The poor DR quality achieved by BH t-SNE, with the same $\overline{\text{AUC}}$ for all three thresholds, suggests that it is far from convergence, before θ starts influencing the LD positioning. On the other hand, FMs t-SNE delivers fair $\overline{\text{AUC}}$, for instance, in 4.5 h on average on Gas, containing almost one million samples. The 2-D embeddings of this data set illustrate in Fig. 7 these results: the LDS computed by FMs t-SNE in Fig. 7(a) indeed reveals a structure related to the three classes of Gas. Such an organization is not obtained by BH t-SNE in Fig. 7(b) and (c), which hardly and fuzzily arrange the data points regardless of the BH threshold θ, leading to a weak $\overline{\text{AUC}}$.

Fig. 8 further shows the results given in Table III. For Shuttle and Sensorless, FMs t-SNE indeed lies in the top-left corner of the figure, whereas BH t-SNE is the fastest on Sgemm, Covertype, and Gas, but with poor $\overline{\text{AUC}}$ compared to FMs t-SNE. It is noteworthy that FMs t-SNE has a less stable $\overline{\text{AUC}}$ on Gas across the random subsamplings compared to all other data sets, due to the challenging nature and large size of Gas.

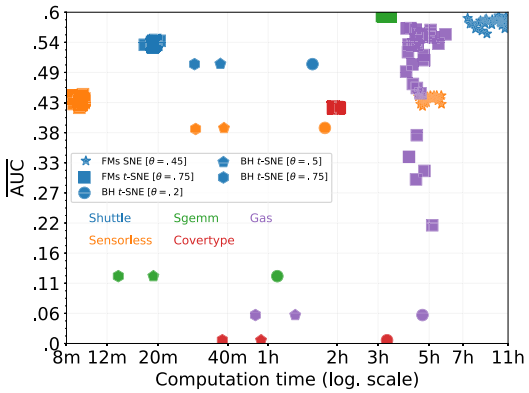

Fig. 8. $\overline{\text{AUC}}$ of the fast DR methods on large-scale data sets, with m and h referring to minute and hour. Results of FMs SNE and FMs t-SNE are depicted for 30 different random subsamplings. The markers and colors, respectively, differentiate the DR methods and data sets. The data sets names are indicated using their associated colors to enable their identification. Contrasts best viewed using colors.

V. Conclusion

In DR, NE methods produce LD versions of HD data sets retaining HD neighborhoods impressively well. HD structures extraction drives a lot of attention, leading to efficient frameworks easing subsequent classification [54]–[56] and clustering [57]–[59]. In visualization, multiscale schemes outperform single-scale ones by accounting for both local and global data interactions, improving the HD neighborhood preservation. Yet, their $\mathcal{O}(N^2 \log N)$ time complexity with N samples limits their applicability to a few thousands data. To tackle larger databases, this article develops $\mathcal{O}(N \log^2 N)$ accelerations of the multiscale NE methods. While fast single-scale methods harness the intrinsic sparsity of their HD similarities, the proposed fast multiscale schemes account for the dense nature of the multiscale HD similarities by defining neighbor sets for each datum incorporating samples summarizing the data cloud from different perspectives. These sets gather the closest HD neighbors to each datum to accurately capture the locally fluctuating structures, as well as HD points sampled with different resolutions to consider the global data cloud properties. With a BH algorithm avoiding LD crushing, the accounted subsets of HD data interactions enable relevantly scoring the LD coordinates quality. The LDS is hence efficiently shaped to reproduce HD relationships at all scales. Although the presented algorithms evolve in $\mathcal{O}(N \log^2 N)$, it is noteworthy that the gradient of FMs t-SNE is iteratively estimated in $\mathcal{O}(N \log N)$ average time. As it requires a single-tree traversal per datum for each gradient approximation, it is superior to FMs SNE, as confirmed experimentally. Simulations highlight that fast multiscale methods consistently and statistically significantly outperform state-of-the-art single-scale schemes in DR quality, while tremendously accelerating their non-fast versions, enabling multiscale visualization of large data sets.

In extremely HD spaces, the efficiency of the nearest neighbor searches through vantage-point trees may decay, due to the curse of dimensionality [1]. In such cases, one can, however, first reduce the dimension with PCA while preserving most information content [32]. Another option is to employ

random projection trees combined with neighbor exploring techniques [35]. As to future lines of work, our methods can be extended to class-aware settings [56], inspired by recent successful works [60]. Weights could also be associated with the multiscale sampled neighbors, proportionally to the number of neglected interactions they represent on average. These interactions would also influence the LDS computation, to improve DR quality. The design of such weights should, however, consider both the HD and LD coordinates, which are iteratively updated. Another perspective is to study FMMs [34] and NSTs [35], to analyze whether they yield better tradeoffs between running time and DR quality. In this line, variants of the BH approximation condition will be investigated as well, according to the alternatives outlined in Appendix A. These refinements would indeed ease meeting the BH approximation launching, hence possibly further reducing computation time without harming the DR performances.

Appendix A
BH Algorithm for t-SNE

The gradient of $C_{\mathrm{t}\star}$ with respect to the LD points extends as

$$\frac{1}{4}\frac{\partial C_{\mathrm{t}\star}}{\partial \mathbf{x}_\upsilon} = \sum_{i\in\mathcal{I}\setminus\{\upsilon\}} (\tau_{\upsilon i\star} - t_{\upsilon i})(\mathbf{x}_\upsilon - \mathbf{x}_i)\left(1+d_{\upsilon i}^2\right)^{-1} \tag{26}$$

$$= \underbrace{\sum_{i\in\mathcal{I}\setminus\{\upsilon\}} \tau_{\upsilon i\star}\frac{\mathbf{x}_\upsilon - \mathbf{x}_i}{1+d_{\upsilon i}^2}}_{\mathbf{f}_\upsilon^{\mathrm{t}\star}} - \underbrace{\frac{\overbrace{\sum_{i\in\mathcal{I}\setminus\{\upsilon\}} \frac{\mathbf{x}_\upsilon - \mathbf{x}_i}{\left(1+d_{\upsilon i}^2\right)^2}}^{\mathbf{g}_\upsilon^{\mathrm{t}}}}{\sum_{k\in\mathcal{I},l\in\mathcal{I}\setminus\{k\}}\left(1+d_{kl}^2\right)^{-1}}}_{g^{\mathrm{t}}}. \tag{27}$$

After replacing $\tau_{\upsilon i\star}$ with $\widetilde{\tau}_{\upsilon i\star}$, the sparsity of $\widetilde{\tau}_{\upsilon i\star}$ enables estimating $\mathbf{f}_\upsilon^{\mathrm{t}\star}$ for all $\upsilon\in\mathcal{I}$ in $\mathcal{O}(K_\star N)$ time. To estimate $\mathbf{g}_\upsilon^{\mathrm{t}}/g^{\mathrm{t}}$. for all $\upsilon\in\mathcal{I}$ in less than $\mathcal{O}\left(N^2\right)$ time, first note that if $d_{ij}\ll d_{\upsilon i}\approx d_{\upsilon j}$, then $t_{\upsilon i}\approx t_{\upsilon j}$ [32]. To benefit from this observation and as the LD dimension P is small in visualization tasks, a quad- ($P=2$) or octree ($P=3$) can be constructed on $\mathbf{X}$ in $\mathcal{O}(N)$ time [32], as shown in Fig. 1(a). Each node of the tree is associated with a rectangular cell in the LDS, the root containing the whole LD embedding. Each nonleaf node has four ($P=2$) or eight ($P=3$) children partitioning the cell into four or eight equal parts at its corners. A leaf contains at most one LD point. For each cell c, let $\mathcal{T}_c\subset\mathcal{I}$ index the LD points inside it. In the node related to c, one can store $\left|\mathcal{T}_c\right|$ and the center of mass $\mathbf{m}_c := \left(1/\left|\mathcal{T}_c\right|\right)\sum_{i\in\mathcal{T}_c}\mathbf{x}_i$ of the points indexed in $\mathcal{T}_c$. Creating the quadtree or octree consists in inserting the LD points one after the other, dividing leafs as soon as they contain two LD points while updating $\left|\mathcal{T}_c\right|$ and $\mathbf{m}_c$ of the traversed nodes [32]. Quadtrees can be generalized to any dimension P but are not suitable to large ones, as the number of children per node grows exponentially with P.

Once the tree defined, a depth-first search enables estimating $\mathbf{g}_\upsilon^{\mathrm{t}}$ in $\mathcal{O}(\log N)$ average time, if the splits in the tree partition the data into roughly equal parts [33]. At each node with associated cell c during the traversal, one determines whether the terms over $\mathcal{T}_c$ in $\mathbf{g}_\upsilon^{\mathrm{t}}$ are similar to each other, which happens when the cell c is sufficiently small and far enough from $\mathbf{x}_\upsilon$, in light of the above observation ($d_{ij}\ll d_{\upsilon i}\approx d_{\upsilon j}$ with i and j in $\mathcal{T}_c$). The condition [38]

$$r_c/d_{\upsilon,\mathbf{m}_c} < \theta \tag{28}$$

formalizes this idea, with r_c the cell diagonal length, $d_{\upsilon,\mathbf{m}_c}$ the LD distance between $\mathbf{x}_\upsilon$ and $\mathbf{m}_c$, and $\theta\in[0,1]$ a user-defined threshold parameter trading off accuracy and speed. One could also replace r_c in (28) with the average distance between $\mathbf{m}_c$ and the LD points indexed in $\mathcal{T}_c$ or the diagonal of the smallest box in cell c which contains all points in $\mathcal{T}_c$. These quantities can be easily derived in $\mathcal{O}(N\log N)$ time and when creating the tree and could improve the tradeoff between computation time and DR quality.

As soon as (28) holds, the depth-first search stops and the part of $\mathbf{g}_\upsilon^{\mathrm{t}}$ over $\mathcal{T}_c$ is estimated as

$$\sum_{i\in\mathcal{T}_c}\frac{\mathbf{x}_\upsilon - \mathbf{x}_i}{\left(1+d_{\upsilon i}^2\right)^2} \approx \left|\mathcal{T}_c\right|\frac{\mathbf{x}_\upsilon - \mathbf{m}_c}{\left(1+d_{\upsilon,\mathbf{m}_c}^2\right)^2} \tag{29}$$

since the terms over $\mathcal{T}_c$ are similar to each other and hence close to their approximation using $\mathbf{m}_c$ as representative for the LD points indexed in $\mathcal{T}_c$. During the same traversal, one can also estimate the sum $g_\upsilon^{\mathrm{t}} := \sum_{l\in\mathcal{I}\setminus\{\upsilon\}} 1/(1+d_{\upsilon l}^2)$. After completing N passes, approximations $\widetilde{\mathbf{g}}_\upsilon^{\mathrm{t}}$ and $\widetilde{g}_\upsilon^{\mathrm{t}}$ of $\mathbf{g}_\upsilon^{\mathrm{t}}$ and g_υ^{t} are available for all $\upsilon\in\mathcal{I}$. The sum $\widetilde{g}^{\mathrm{t}} := \sum_{\upsilon\in\mathcal{I}}\widetilde{g}_\upsilon^{\mathrm{t}}$ estimates g^{t}. Since each traversal costs $\mathcal{O}(\log N)$ average time, $\widetilde{g}^{\mathrm{t}}$ and $\widetilde{\mathbf{g}}_\upsilon^{\mathrm{t}}$ for all $\upsilon\in\mathcal{I}$ are obtained in $\mathcal{O}(N\log N)$ average time.

Fig. 1 shows the computation of $\widetilde{\mathbf{g}}_\upsilon^{\mathrm{t}}$ and $\widetilde{g}_\upsilon^{\mathrm{t}}$. The square data point corresponds to $\mathbf{x}_\upsilon$ in Fig. 1(b) and (c). Fig. 1(b) computes $\mathbf{g}_\upsilon^{\mathrm{t}}$ and g_υ^{t} exactly, leading to $\mathcal{O}\left(N^2\right)$ time complexity when performed for all $\upsilon\in\mathcal{I}$. Fig. 1(c) sketches their BH approximation in $\mathcal{O}(\log N)$ average time, in which the centers of mass of the LD points in farther cells to $\mathbf{x}_\upsilon$ summarize their contributions in $\mathbf{g}_\upsilon^{\mathrm{t}}$ and g_υ^{t}.

Appendix B
BH Algorithm for Multiscale SNE

The gradient of (21) with respect to the LD points writes

$$H\frac{\partial\widetilde{C}}{\partial\mathbf{x}_\upsilon} = \sum_{i\in\mathcal{I}\setminus\{\upsilon\}}\underbrace{\left(\sum_{h=1}^{H}p_h s_{\upsilon ih}\right)}_{f_{\upsilon i}}\frac{\widetilde{\sigma}_{\upsilon i}}{s_{\upsilon i}}(\mathbf{x}_\upsilon - \mathbf{x}_i) \tag{30}$$

$$- \sum_{h=1}^{H}p_h\underbrace{\left[\sum_{i\in\mathcal{I}\setminus\{\upsilon\}}\frac{\widetilde{\sigma}_{\upsilon i}}{s_{\upsilon i}}s_{\upsilon ih}\right]}_{g_{\upsilon h}}\underbrace{\left[\sum_{i\in\mathcal{I}\setminus\{\upsilon\}}s_{\upsilon ih}(\mathbf{x}_\upsilon - \mathbf{x}_i)\right]}_{\mathbf{g}_{\upsilon h}} \tag{31}$$

$$+ \sum_{i\in\mathcal{I}\setminus\{\upsilon\}}\underbrace{\left(\sum_{h=1}^{H}p_h s_{i\upsilon h}\right)}_{f_{i\upsilon}}\frac{\widetilde{\sigma}_{i\upsilon}}{s_{i\upsilon}}(\mathbf{x}_\upsilon - \mathbf{x}_i) \tag{32}$$

$$- \sum_{h=1}^{H}p_h\sum_{i\in\mathcal{I}\setminus\{\upsilon\}}s_{i\upsilon h}(\mathbf{x}_\upsilon - \mathbf{x}_i)\underbrace{\left[\sum_{j\in\mathcal{I}\setminus\{i\}}\frac{\widetilde{\sigma}_{ij}}{s_{ij}}s_{ijh}\right]}_{g_{ih}}. \tag{33}$$

The denominator of (9), $\bar{s}_{ih} := \sum_{k\in\mathcal{I}\setminus\{i\}} \exp(-p_h d_{ik}^2/2)$, can first be estimated for all $i \in \mathcal{I}$ and $h = 1,\ldots,H$ in $\mathcal{O}\big(N\log^2 N\big)$ average time by extending the BH algorithm from Appendix A. Then, f_{vi} and s_{vi} can be approximated for all $v \in \mathcal{I}$ and $i \in \widetilde{\mathcal{I}}_v$ in $\mathcal{O}\big(N\log^2 N\big)$ time as $\big|\widetilde{\mathcal{I}}_v\big|$ is $\mathcal{O}(\log N)$. Afterward, estimating the right-hand side of (30) for all $v \in \mathcal{I}$ takes $\mathcal{O}(N\log N)$ time, due to the sparsity of $\widetilde{\sigma}_{vi}$ that reduces the sum over $\mathcal{I}\setminus\{v\}$ to a sum over $\widetilde{\mathcal{I}}_v$. Similarly, (32) is approximated for all $v \in \mathcal{I}$ in $\mathcal{O}(N\log N)$ time and g_{vh} for all $v \in \mathcal{I}$ and $h = 1,\ldots,H$ in $\mathcal{O}\big(N\log^2 N\big)$ time. On the other hand, $\mathbf{g}_{vh}$ satisfies

$$\bar{s}_{vh}\mathbf{g}_{vh} = \sum_{i\in\mathcal{I}\setminus\{v\}} \exp\big(-p_h d_{vi}^2/2\big)(\mathbf{x}_v - \mathbf{x}_i) \tag{34}$$

where the right-hand side is estimated in $\mathcal{O}(\log N)$ average time due to the BH algorithm. Thus, (31) is estimated for all $v \in \mathcal{I}$ in $\mathcal{O}\big(N\log^2 N\big)$ average time. Finally, (33) extends as

$$\sum_{i\in\mathcal{I}\setminus\{v\}} \left[\sum_{h=1}^{H} p_h \exp(-p_h d_{iv}^2/2)\frac{g_{ih}}{\bar{s}_{ih}}\right](\mathbf{x}_v - \mathbf{x}_i). \tag{35}$$

To approximate (35), the quadtree is extended by storing, in each cell c, $\mathcal{O}(\log N)$ additional attributes consisting of

$$a_h^c := \big|\mathcal{T}_c\big|^{-1} \sum_{i\in\mathcal{T}_c} g_{ih}/\bar{s}_{ih} \tag{36}$$

for $h = 1,\ldots,H$, yielding a tree with $\mathcal{O}(N\log N)$ memory cost [33]. Depth-first searching the resulting tree enables estimating (35) in $\mathcal{O}\big(\log^2 N\big)$ average time, by stopping the traversal as soon as (28) holds and approximating the part of (35) with $i \in \mathcal{T}_c$ through a sum of $\mathcal{O}(\log N)$ terms

$$\big|\mathcal{T}_c\big|\left[\sum_{h=1}^{H} p_h \exp(-p_h d_{v,\mathbf{m}_c}^2/2)a_h^c\right](\mathbf{x}_v - \mathbf{m}_c). \tag{37}$$

Estimating (33) for all $v \in \mathcal{I}$ hence takes $\mathcal{O}\big(N\log^2 N\big)$ average time, which is the time complexity of approximating the gradient of (21). It is noteworthy that the estimation entails two tree traversals for each $v \in \mathcal{I}$, to first approximate (30)–(32) and (36) and then estimate (33) during the second search.

REFERENCES

[1] J. A. Lee and M. Verleysen, *Nonlinear Dimensionality Reduction*. New York, NY, USA: Springer, 2007.

[2] X. Li, H. Zhang, R. Zhang, Y. Liu, and F. Nie, "Generalized uncorrelated regression with adaptive graph for unsupervised feature selection," *IEEE Trans. Neural Netw. Learn. Syst.*, vol. 30, no. 5, pp. 1587–1595, May 2019.

[3] R. Zhang, F. Nie, Y. Wang, and X. Li, "Unsupervised feature selection via adaptive multimeasure fusion," *IEEE Trans. Neural Netw. Learn. Syst.*, vol. 30, no. 9, pp. 2886–2892, Sep. 2019.

[4] I. Borg and P. J. F. Groenen, *Modern Multidimensional Scaling: Theory and Applications*. New York, NY, USA: Springer, 2005.

[5] T. Kohonen, "The self-organizing map," *Proc. IEEE*, vol. 78, no. 9, pp. 1464–1480, Sep. 1990.

[6] G. Hinton and S. Roweis, "Stochastic neighbor embedding," in *Proc. NIPS*, vol. 15, 2002, pp. 857–864.

[7] I. T. Jolliffe, "Principal component analysis and factor analysis," in *Principal Component Analysis*. New York, NY, USA: Springer, 1986, pp. 115–128.

[8] J. W. Sammon, "A nonlinear mapping for data structure analysis," *IEEE Trans. Comput.*, vol. C-18, no. 5, pp. 401–409, May 1969.

[9] J. B. Tenenbaum, "A global geometric framework for nonlinear dimensionality reduction," *Science*, vol. 290, no. 5500, pp. 2319–2323, Dec. 2000, doi: 10.1126/science.290.5500.2319.

[10] M. Belkin and P. Niyogi, "Laplacian eigenmaps and spectral techniques for embedding and clustering," in *Adv. neural Inf. Process. Syst.*, 2002, pp. 585–591.

[11] S. T. Roweis, "Nonlinear dimensionality reduction by locally linear embedding," *Science*, vol. 290, no. 5500, pp. 2323–2326, Dec. 2000, doi: 10.1126/science.290.5500.2323.

[12] J. A. Lee and M. Verleysen, "Quality assessment of dimensionality reduction: Rank-based criteria," *Neurocomputing*, vol. 72, nos. 7–9, pp. 1431–1443, Mar. 2009.

[13] L. van der Maaten and G. Hinton, "Visualizing data using t-SNE," *J. Mach. Learn. Res.*, vol. 9, pp. 2579–2605, Nov. 2008.

[14] B. Schölkopf, A. Smola, and K.-R. Müller, "Nonlinear component analysis as a kernel eigenvalue problem," *Neural Comput.*, vol. 10, no. 5, pp. 1299–1319, Jul. 1998.

[15] D. Francois, V. Wertz, and M. Verleysen, "The concentration of fractional distances," *IEEE Trans. Knowl. Data Eng.*, vol. 19, no. 7, pp. 873–886, Jul. 2007.

[16] J. A. Lee and M. Verleysen, "Shift-invariant similarities circumvent distance concentration in stochastic neighbor embedding and variants," *Procedia Comput. Sci.*, vol. 4, pp. 538–547, 2011.

[17] J. Venna, J. Peltonen, K. Nybo, H. Aidos, and S. Kaski, "Information retrieval perspective to nonlinear dimensionality reduction for data visualization," *J. Mach. Learn. Res.*, vol. 11, pp. 451–490, Feb. 2010.

[18] Z. Yang, I. King, Z. Xu, and E. Oja, "Heavy-tailed symmetric stochastic neighbor embedding," in *Proc. NIPS*, 2009, pp. 2169–2177.

[19] C. de Bodt, D. Mulders, D. López-Sánchez, M. Verleysen, and J. A. Lee, "Class-aware t-SNE: Cat-SNE," in *Proc. ESANN*, 2019, pp. 409–414.

[20] K. Bunte, S. Haase, M. Biehl, and T. Villmann, "Stochastic neighbor embedding (SNE) for dimension reduction and visualization using arbitrary divergences," *Neurocomputing*, vol. 90, pp. 23–45, Aug. 2012.

[21] J. A. Lee, E. Renard, G. Bernard, P. Dupont, and M. Verleysen, "Type 1 and 2 mixtures of Kullback–Leibler divergences as cost functions in dimensionality reduction based on similarity preservation," *Neurocomputing*, vol. 112, pp. 92–108, Jul. 2013.

[22] C. de Bodt, D. Mulders, M. Verleysen, and J. A. Lee, "Nonlinear dimensionality reduction with missing data using parametric multiple imputations," *IEEE Trans. Neural Netw. Learn. Syst.*, vol. 30, no. 4, pp. 1166–1179, Apr. 2019, doi: 10.1109/TNNLS.2018.2861891.

[23] M. Carreira-Perpinán, "The elastic embedding algorithm for dimensionality reduction," in *Proc. ICML*, vol. 10, 2010, pp. 167–174.

[24] L. Van Der Maaten, "Fast optimization for t-SNE," in *Proc. NIPS Workshop Challenges Data Vis.*, 2010, pp. 1–5.

[25] M. Vladymyrov and M. Carreira-Perpinán, "Entropic affinities: Properties and efficient numerical computation," in *Proc. ICML*, 2013, pp. 477–485.

[26] M. Vladymyrov and M. Carreira-Perpinan, "Partial-Hessian strategies for fast learning of nonlinear embeddings," in *Proc. ICML*, vol. 29, 2012, pp. 345–352.

[27] J. A. Lee, D. H. Peluffo-Ordóñez, and M. Verleysen, "Multi-scale similarities in stochastic neighbour embedding: Reducing dimensionality while preserving both local and global structure," *Neurocomputing*, vol. 169, pp. 246–261, Dec. 2015.

[28] C. de Bodt, D. Mulders, M. Verleysen, and J. A. Lee, "Perplexity-free t-SNE and twice student tt-SNE," in *Proc. ESANN*, 2018, pp. 123–128.

[29] J. Peltonen and K. Georgatzis, "Efficient optimization for data visualization as an information retrieval task," in *Proc. IEEE Int. Workshop Mach. Learn. Signal Process.*, Santander, Spain, Sep. 2012, pp. 1–6.

[30] L. V. D. Maaten, "Learning a parametric embedding by preserving local structure," in *Proc. Artif. Intell. Statist.*, 2009, pp. 384–391.

[31] F. Crecchi, C. de Bodt, M. Verleysen, J. A. Lee, and D. Bacciu, "Perplexity-free Parametric t-SNE," in *Proc. ESANN*, 2020, pp. 387–392.

[32] L. van der Maaten, "Accelerating t-SNE using tree-based algorithms," *J. Mach. Learn. Res.*, vol. 15, no. 1, pp. 3221–3245, Oct. 2014.

[33] Z. Yang, J. Peltonen, and S. Kaski, "Scalable optimization of neighbor embedding for visualization," in *Proc. ICML*, vol. 2, 2013, pp. 127–135.

[34] M. Vladymyrov and M. Carreira-Perpinan, "Linear-time training of nonlinear low-dimensional embeddings," in *Proc. Artif. Intell. Statist.*, 2014, pp. 968–977.

[35] J. Tang, J. Liu, M. Zhang, and Q. Mei, "Visualizing large-scale and high-dimensional data," in *Proc. 25th Int. Conf. World Wide Web*, Apr. 2016, pp. 287–297.

[36] C. Bouveyron, S. Girard, and C. Schmid, "High-dimensional data clustering," *Comput. Statist. Data Anal.*, vol. 52, no. 1, pp. 502–519, 2007.

[37] P. Yianilos, "Data structures and algorithms for nearest neighbor search in general metric spaces," in *Proc. SODA*, 1993, vol. 93, no. 194, pp. 311–321.
[38] J. Barnes and P. Hut, "A hierarchical O(N log N) force-calculation algorithm," *Nature*, vol. 324, no. 6096, pp. 446–449, 1986.
[39] C. de Bodt, D. Mulders, M. Verleysen, and J. A. Lee, "Extensive assessment of Barnes-Hut t-SNE," in *Proc. ESANN*, 2018, pp. 135–140.
[40] R. B. D'Agostino, "An omnibus test of normality for moderate and large size samples," *Biometrika*, vol. 58, no. 2, pp. 341–348, 1971.
[41] J. P. Shaffer, "Multiple hypothesis testing," *Annu. Rev. Psychol.*, vol. 46, no. 1, pp. 561–584, 1995.
[42] R. H. Byrd, P. Lu, J. Nocedal, and C. Zhu, "A limited memory algorithm for bound constrained optimization," *SIAM J. Scientific Comput.*, vol. 16, no. 5, pp. 1190–1208, Sep. 1995.
[43] M. Lichman. (2013). *UCI Machine Learning Repository*. [Online]. Available: http://archive.ics.uci.edu/ml
[44] P. Tüfekci, "Prediction of full load electrical power output of a base load operated combined cycle power plant using machine learning methods," *Int. J. Electr. Power Energy Syst.*, vol. 60, pp. 126–140, Sep. 2014.
[45] H. Kaya, P. Tüfekci, and S. F. Gürgen, "Local and global learning methods for predicting power of a combined gas & steam turbine," in *Proc. Int. Conf. ETCEE*, 2012, pp. 13–18.
[46] R. Madeo, C. Lima, and S. Peres, "Gesture unit segmentation using support vector machines: Segmenting gestures from rest positions," in *Proc. 28th Annu. ACM Symp. Appl. Comput.*, 2013, pp. 46–52.
[47] J. Bridge, S. Holden, and L. Paulson, "Machine learning for first-order theorem proving: Learning to select a good heuristic," *J. Automated Reasoning*, vol. 53, no. 2, pp. 141–172, 2014.
[48] I. Guyon, S. Gunn, A. Ben-Hur, and G. Dror, "Result analysis of the NIPS 2003 feature selection challenge," in *Proc. NIPS*, 2004, pp. 545–552.
[49] P. Cortez, A. Cerdeira, F. Almeida, T. Matos, and J. Reis, "Modeling wine preferences by data mining from physicochemical properties," *Decis. Support Syst.*, vol. 47, no. 4, pp. 547–553, Nov. 2009.
[50] L. Chen and A. Buja, "Local multidimensional scaling for nonlinear dimension reduction, graph drawing, and proximity analysis," *J. Amer. Stat. Assoc.*, vol. 104, no. 485, pp. 209–219, Mar. 2009.
[51] B. Mokbel, W. Lueks, A. Gisbrecht, and B. Hammer, "Visualizing the quality of dimensionality reduction," *Neurocomputing*, vol. 112, pp. 109–123, Jul. 2013.
[52] C. Nugteren and V. Codreanu, "CLTune: A generic auto-tuner for OpenCL kernels," in *Proc. IEEE 9th Int. Symp. Embedded Multicore/Many-Core Syst.–Chip*, Sep. 2015, pp. 195–202.
[53] R. Huerta, T. Mosqueiro, J. Fonollosa, N. F. Rulkov, and I. Rodriguez-Lujan, "Online decorrelation of humidity and temperature in chemical sensors for continuous monitoring," *Chemometric Intell. Lab. Syst.*, vol. 157, pp. 169–176, Oct. 2016.
[54] R. Zhang, F. Nie, and X. Li, "Self-weighted supervised discriminative feature selection," *IEEE Trans. Neural Netw. Learn. Syst.*, vol. 29, no. 8, pp. 3913–3918, Aug. 2018.
[55] R. Zhang, F. Nie, and X. Li, "Semisupervised learning with parameter-free similarity of label and side information," *IEEE Trans. Neural Netw. Learn. Syst.*, vol. 30, no. 2, pp. 405–414, Feb. 2019.
[56] R. Zhang, F. Nie, and X. Li, "Regularized class-specific subspace classifier," *IEEE Trans. Neural Netw. Learn. Syst.*, vol. 28, no. 11, pp. 2738–2747, Nov. 2017.
[57] R. Zhang, F. Nie, M. Guo, X. Wei, and X. Li, "Joint learning of fuzzy k-means and nonnegative spectral clustering with side information," *IEEE Trans. Image Process.*, vol. 28, no. 5, pp. 2152–2162, May 2019.
[58] K. Zhang, X. Gao, D. Tao, and X. Li, "Single image super-resolution with multiscale similarity learning," *IEEE Trans. Neural Netw. Learn. Syst.*, vol. 24, no. 10, pp. 1648–1659, Oct. 2013.
[59] X. Gao, K. Zhang, D. Tao, and X. Li, "Image super-resolution with sparse neighbor embedding," *IEEE Trans. Image Process.*, vol. 21, no. 7, pp. 3194–3205, Jul. 2012.
[60] Y. Liu, R. Zhang, F. Nie, X. Li, and C. Ding, "Supervised dimensionality reduction methods via recursive regression," *IEEE Trans. Neural Netw. Learn. Syst.*, vol. 31, no. 9, pp. 3269–3279, Sep. 2020, doi: 10.1109/TNNLS.2019.2940088.

Cyril de Bodt was born in Brussels, Belgium, in 1993. He received the M.Sc. degree in applied sciences (mathematical engineering) and the Ph.D. degree in engineering science and technology from the Université catholique de Louvain (UCLouvain), Louvain-la-Neuve, Belgium, in 2016 and 2020, respectively.

He is currently a Post-Doctoral Research Fellow with the Human Dynamics Group, Massachusetts Institute of Technology (MIT) Media Lab, Cambridge, MA, USA. His research interests include dimensionality reduction, machine learning, visualization, clustering, optimization, and data mining.

Dounia Mulders was born in Liege, Belgium, in 1993. She received the M.Sc. degree in applied sciences (mathematical engineering) and the Ph.D. degree in engineering science and technology from the Université catholique de Louvain (UCLouvain), Louvain-la-Neuve, Belgium, in 2016 and 2020, respectively.

As a Post-Doctoral Research Fellow at the Fiete Lab, Department of Brain and Cognitive Sciences, Massachusetts Institute of Technology (MIT), Cambridge, MA, USA, she studies the central mechanisms of pain perception in humans using signal processing and machine learning tools to analyze scalp and intracerebral EEG recordings.

Michel Verleysen (Fellow, IEEE) has been an Invited Professor with the Swiss Federal Institute of Technology Lausanne, Lausanne, Switzerland; the Université d'Evry Val d'Essonne, Évry-Courcouronnes, France; the Université ParisI-Panthéon-Sorbonne, Paris, France; and the Université Paris-Est, Champs-sur-Marne, France. He is currently a Professor of machine learning with the Université catholique de Louvain (UCLouvain), Louvain-la-Neuve, Belgium. He is an Honorary Research Director of the Belgian FNRS and the Dean of the Louvain School of Engineering. He is the author of more than 250 scientific articles in international journals, books, or peer-reviewed conferences. His research interests include machine learning, feature selection, dimensionality reduction, visualization, high-dimensional data analysis, self-organization, time-series forecasting, and biomedical signal processing.

Prof. Verleysen was the Chairman of the IEEE Computational Intelligence Society Benelux Chapter from 2008 to 2010 and a member of the Executive Board of the European Neural Networks Society from 2005 to 2010. He is the Editor-in-Chief of the *Neural Processing Letters* journal, the chairman of the annual ESANN conference, a past Associate Editor of the IEEE TRANSACTIONS ON NEURAL NETWORKS, and a member of the Editorial Board and a program committee of several journals and conferences on neural networks and learning.

John Aldo Lee was born in Brussels, Belgium, in 1976. He received the M.Sc. degree in computer engineering and the Ph.D. degree in machine learning from the Université catholique de Louvain (UCLouvain), Louvain-la-Neuve, Belgium, in 1999 and 2003, respectively.

He is currently a member of the UCLouvain Machine Learning Group and a Senior Research Associate with the Belgian FNRS. He is also working with the UCLouvain Center of Molecular Imaging, Radiotherapy, and Oncology (MIRO), where he develops specific image processing techniques to improve and speed up treatment planning in radiation oncology. He has authored a monography entitled *Nonlinear Dimensionality Reduction* (Springer, 2007) together with Michel Verleysen. His main research interests are dimensionality reduction, clustering, vector quantization, and various aspects of image processing applied to cancer care.